Image Cover Sheet

CLASSIFICATION	SYSTEM NUMBER
UNCLASSIFIED	508328

TITLE

IR FOURIER SPECTROMETER FOR DIFFERENTIAL DETECTION: DESIGN, PROTOTYPE AND RESULTS

System Number:

Patron Number:

Requester:

Notes:

DSIS Use only:

Deliver to:

DEFENCE RESEARCH ESTABLISHMENT
CENTRE DE RECHERCHES POUR LA DÉFENSE
VALCARTIER, QUÉBEC

DREV - R - 9804
Unlimited Distribution / Distribution illimitée

IR FOURIER SPECTROMETER FOR DIFFERENTIAL DETECTION: DESIGN, PROTOTYPE AND RESULTS

by

Jean-Marc Thériault

June / juin 1998

RESEARCH AND DEVELOPMENT BRANCH
DEPARTMENT OF NATIONAL DEFENCE
CANADA
BUREAU - RECHERCHE ET DÉVELOPPEMENT
MINISTÈRE DE LA DÉFENSE NATIONALE

UNCLASSIFIED

DEFENCE RESEARCH ESTABLISHMENT
CENTRE DE RECHERCHES POUR LA DÉFENSE
VALCARTIER, QUÉBEC

DREV - R - 9804
Unlimited Distribution / Distribution illimitée

IR FOURIER SPECTROMETER FOR DIFFERENTIAL DETECTION: DESIGN, PROTOTYPE AND RESULTS

by

Jean-Marc Thériault

June / juin 1998

Approved by / approuvé par

Section Head / Chef de section

29 May 98
Date

SANS CLASSIFICATION

ABSTRACT

This report presents the theoretical basis and validation measurements supporting a new configuration of Fourier-transform IR spectrometer optimized for differential detection. The optimized configuration exploits the optical subtraction capabilities of a double-beam Michelson interferometer. It has been designed to satisfy two requirements, the suppression of the spectral background, which overlays the desired spectral signature, and the suppression of the internal IR emission contributions arising from the spectrometer itself. The resulting configuration is a fully symmetrical FTIR double-beam interferometer with a special beamsplitter assembly. To verify the proposed design a prototype has been developed and tested experimentally. The results obtained with this prototype indicate a high level of suppression with a residual usually smaller than 2 % in the spectral range from 3.5 to 15 μm. The analysis of the results indicates that the remaining residual can be explained by small dissymetries in transmittance and thickness of the two ZnSe substrates forming the beamsplitter. Finally, this spectrometer configuration allows a permanent radiometric calibration, which represents a definitive advantage over conventional FTIR instruments.

RÉSUMÉ

Ce rapport présente les bases théoriques et les mesures de validation qui sous-tend une une nouvelle configuration de spectromètre IR par transformation de Fourier (FTIR) qui est optimisée pour la détection différentielle. Cette configuration optimisée exploite les capacités de soustraction optique de l'interféromètre de Michelson à double entrée. Il a été conçu de manière à satisfaire deux impératifs, la suppression de l'arrière-plan spectral qui masque la signature désirée et la suppression de l'émission IR auto-induite par le spectromètre. La configuration résultante est un interféromètre FTIR à double entrée parfaitement symétrique muni d'un dispositif particulier de lames séparatrices. Afin d'évaluer le design proposé, un prototype a été mis au point et vérifié expérimentalement. Les résultats obtenus avec ce prototype indiquent un degré élevé de suppression avec un résidu inférieur à 2 % dans la région spectrale 3,5 à 15 μm. L'analyse des résultats indique que ce résidu peut s'expliquer par de petites dissymétries entre les transmissions et les épaisseurs des deux substrats formant le dispositif séparateur. Finalement, cette configuration de spectromètre permet un étalonnage radiométrique permanent, ce qui représente un avantage marqué sur les spectromètres FTIR conventionnels.

TABLE OF CONTENTS

EXECUTIVE SUMMARY

The Canadian Forces are using a variety of electro-optical systems for the remote sensing of target characteristics. In the past few years, the development of passive IR spectral sensors has grown to a point at which it is now considered a vital technology for the remote monitoring of battlefield environment, providing unique information on the ongoing maneuvers. For instance, one of the most promising applications in passive spectral surveillance is the remote detection and identification of toxic vapors. It has been shown that such a detection can be performed remotely using a Fourier Transform InfraRed (FTIR) spectrometer which probes the IR emission spectra of the associated gases. This technique was originally conceived to provide ground soldiers with an early warning of chemical threats.

Defence Research Establishment Valcartier (DREV) is currently developing a passive FTIR technique for the passive remote monitoring of battlefield gaseous emissions. There are two known difficulties encountered in the application of such a technique. First, it requires the suppression of the spectral background which overlays the desired spectral signature. Second, it requires the handling of the internal IR emission arising from the spectrometer itself. To overcome these two limitations DREV has recently proposed a novel approach of differential detection based on a specially designed double-beam FTIR spectrometer. In this system, two beams coming from different scenes can be spatially combined on a single detector and optically subtracted in real-time. Thus if one beam entering the interferometer corresponds to the target-plus-background scene and the other beam corresponds to the surrounding background, then the resulting spectrum is free of background and self-instrument emission. This capability is particularly suited for the detection of weak IR emission signatures in a strong atmospheric background.

This report presents the theoretical basis and the validation measurements supporting the design of the proposed double-beam FTIR spectrometer for differential detection. The research effort has been concentrated in formulating the proper requirements for an optimized configuration and finding practical solutions. In particular, to achieve these requirements it has been proposed to use a fully symmetrical FTIR double-beam interferometer with a special beamsplitter assembly. To verify the proposed configuration a prototype has been developed and tested. The results obtained with this prototype indicate a high level of suppression with an instrument residual usually smaller than 2 % in the spectral range from 3.5 to 15 μm. Moreover, it has been found that this configuration permits a permanent radiometric calibration, which represents a definitive advantage over conventional FTIR instrument for real-time sensing.

The results of this work may also have a significant impact on several other remote sensing applications involving atmospheric pollution monitoring from the ground or from an airborne platform. In addition, this work contributes directly to Canadian inputs to TTCP JTP-13 and NATO RSG-8 international technical groups.

1.0 INTRODUCTION

There exist a variety of electro-optical (EO) sensors being developed to assist the Canadian Forces in surveillance operations. Among them, passive IR spectral sensors appear to become a vital technology for the remote sensing of battlefield environment which can provide unique information on the ongoing maneuvers. For instance, spectral information might be used to remotely probe different types of equipment, camouflages, smokes and clothing. One of the most promising military application in passive spectral surveillance is the remote detection and identification of toxic vapors. It was originally conceived to provide ground soldiers with an early warning of chemical threats. It has been shown that such a detection can be performed remotely using a Fourier Transform InfraRed (FTIR) spectrometer which probes the IR emission spectra of the associated gases (Refs. 1-3). However, there are two main difficulties associated with such a passive spectral technique. First, it requires the suppression of the spectral background which overlays the desired spectral signature, and second, it requires the handling of the internal IR emission arising from the spectrometer itself. In this report we propose an approach to address these two limitations.

Defence Research Establishment Valcartier (DREV) is currently developing a passive FTIR technique for the passive remote monitoring of battlefield gaseous emissions. The DREV approach takes advantage of the differential detection provided by a specially designed FTIR dual-beam interferometer with adjacent fields of view. In this system two beams coming from different scenes can be optically combined on a single detector and subtracted in real-time. Thus, if one beam entering the interferometer corresponds to the target-plus-background scene and the other corresponds to an equivalent surrounding background scene alone then the resulting target spectrum is almost free of background. This is particularly suited for detection of weak IR emission signatures in a strong atmospheric background.

A major limitation encountered with standard FTIR spectrometers is that the output signal contains parasite radiation, i.e. the internal IR emission arising from the spectrometer itself. Consequently, a special calibration procedure involving two reference measurements must be applied to obtain and correct for this self-emission term in addition to the usual responsivity parameter. In current FTIR spectrometers this self-emission term is generally uncontrolled and variable in time. Thus, the best way to acquire radiometrically accurate

spectra is by doing frequent calibration measurements. This constraint of frequent calibration represents a serious burden reducing the efficiency and the applicability of FTIR instrument especially for real-time sensing.

In this report we describe an FTIR spectrometer optimized for the differential detection (Refs. 4-5). This special configuration permits the simultaneous suppression of the spectral background and the instrument self-emission spectrum. In addition it allows a permanent calibration, which represents a definitive advantage for real-time remote sensing. In Chapter 2, we first review some general concepts related to Fourier transform spectrometers (FTS). The proposed FTIR configuration and the related design equations are presented in Chapter 3. In Chapter 4, the theory of optical interference is used to specify a beamsplitter configuration that matches the requirements. In Chapters 5 and 6, the results obtained with a prototype are presented and discussed as a validation of the proposed configuration. Finally, Chapter 7 summarizes the work and draws conclusions on the anticipated performance of this optimized FTIR spectrometer.

This work was performed at DREV between April 1996 and November 1997 under Thrust 2d - Land Forces Tactical Surveillance and Counter-Surveillance, Work Unit 2da25: Gaseous Emission Monitoring for Surveillance: Feasibility Study.

2.0 BACKGROUND INFORMATION

2.1 FTS Generalities

In this section, we review some basic aspects related to Fourier transform tpectrometers. More information on the subject can be found for instance in Ref. 6. The basic characteristic of an FTS is to act as a modulator. The principle is that the interferometer modulates the incident beam intensity according to the wavelength of the radiation. The interferometer most often used is a Michelson. A schematic of this interferometer is presented in Fig. 1. The beam from the source is divided by a beamsplitter (BS) into two separate components which are recombined after traveling different optical path lengths. In a Fourier spectrometer, the Michelson interferometer is designed in a way that one or both of its mirrors can move periodically (note that in Fig. 1, only one mirror is moving) around a mean position creating a periodic optical path difference between the two interfering beams. In this case when a monochromatic radiation of unit amplitude (Fig. 1) is incident on the interferometer the emergent amplitude A(x) is given by

$$A(x) = (r\ t) + (t\ r)\ e^{i\ 2\pi\nu x} \qquad [1]$$

where ν is the wavenumber (inverse of the wavelength, $1/\lambda$), x is the optical path difference between the two interfering beams and r and t represent the amplitude reflection and transmission coefficients of the beamsplitter, respectively. Note that the temporal variation of the amplitude terms in eq. 1 has been neglected assuming an observation time long enough to take the averaged amplitude. This simplified radiation source (monochromatic radiation of unit amplitude) is helpful in establishing the basic characteristic of the instrument, i.e. the optical responsivity K. For the moment we neglect the electronic responsivity. As seen below, the responsivity K depends essentially on the transmission and reflection of the many optical elements encountered in the optical path. By definition, the emerging intensity I(x) is found by multiplication of the amplitude A(x) with its complex conjugate A(x)* yielding

$$I(x) = A(x)\ A^*(x) = 2RT + RT\ (e^{i\ 2\pi\nu x} + e^{-i\ 2\pi\nu x}) \qquad [2]$$

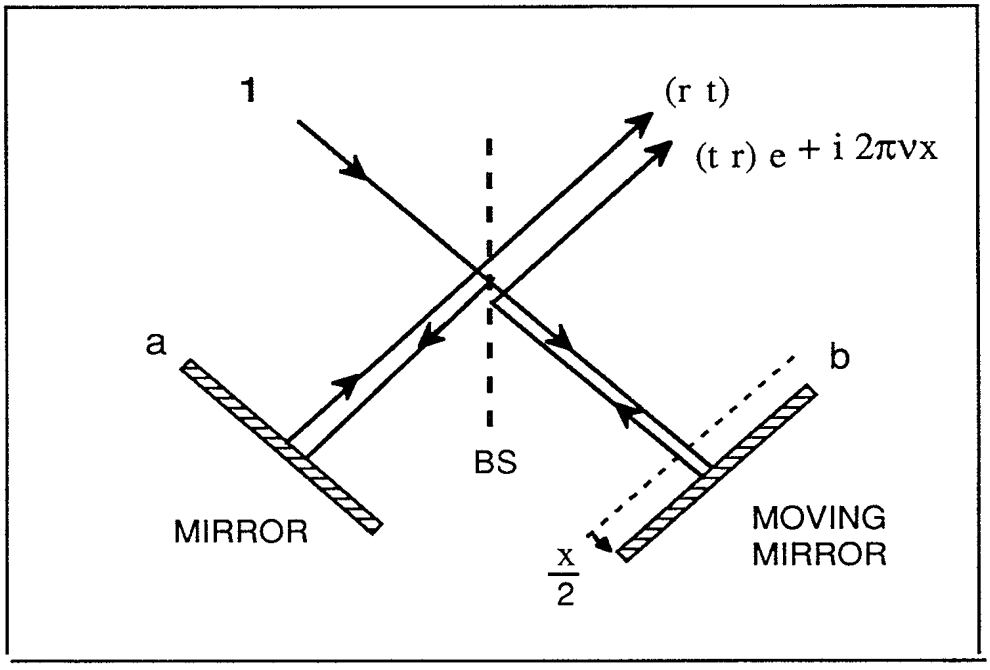

FIGURE 1 - Principle of the Michelson interferometer used as a modulator in a Fourier transform spectrometer

where the beamsplitter reflection and transmission in intensity, R and T are given by (r r*) and (t t*), respectively. The interferogram F(x) is defined as the modulated component of the above intensity, i.e.

$$F(x) = K\,(e^{i\,2\pi\nu x} + e^{-i\,2\pi\nu x}) \qquad [3]$$

and where K = RT has been defined as the optical responsivity. Equation 3 represents the interferogram obtained from a monochromatic source passing through an ideal interferometer.

When a polychromatic beam of intensity B(ν) is incident on a FT interferometer it generates an interferogram that can be represented by the continuous summation of individual modulations associated to each spectral element, i.e.

$$F(x) = \int_0^\infty B(\nu)\,K(\nu)\,(e^{i\,2\pi\nu x} + e^{-i\,2\pi\nu x})\,d\nu\,, \qquad [4]$$

where the responsivity K(ν) is now wavenumber dependent. Using a mathematical artifice (it does not affect the physical representation) which consists in extending the domain of integration to include the negative values of ν and assuming symmetric spectra for B(ν) and K(ν) where

$$B(-\nu) \equiv B(\nu)\,, \qquad [5]$$

and

$$K(-\nu) \equiv K(\nu)\,, \qquad [6]$$

we find, after rearrangement, an interferogram expression more appropriate for processing. In this case and by application of the basic Fourier transform property we have

$$F(x) = \int_{-\infty}^\infty B(\nu)\,K(\nu)\,e^{i\,2\pi\nu x}\,d\nu\,, \qquad [7]$$

and

$$B(\nu)\, K(\nu) = \int_{-\infty}^{\infty} F(x)\, e^{-i\, 2\pi\nu x}\, dx\,. \qquad [8]$$

Equation 7 states that the interferogram F(x) generated by an ideal instrument is given by the inverse Fourier transform of the raw spectrum B(ν) K(ν) while eq. 8 states that the raw spectrum is given by the Fourier transform of the interferogram.

As opposed to an ideal instrument a real interferometer usually introduces an additional phase shift ψ(ν) due to an imperfect compensation from dispersive elements (e.g. substrates of beamsplitter and compensator). In this case the pair of Fourier transform becomes

$$F(x) = \int_{-\infty}^{\infty} \left[B(\nu)\, K(\nu)\, e^{i\,\psi(\nu)}\right] e^{i\, 2\pi\nu x}\, d\nu \qquad [9]$$

and

$$\left[B(\nu)\, K(\nu)\, e^{i\,\psi(\nu)}\right] = \int_{-\infty}^{\infty} F(x)\, e^{-i\, 2\pi\nu x}\, dx\,. \qquad [10]$$

Equation 10 is the basic relation used in Fourier spectroscopy where the complex raw spectrum is simply given by the complex Fourier transform of a real double-sided interferogram. Note that the absolute radiometric spectrum B(ν) is not a direct output and the instrument responsivity must be calibrated from auxiliary measurements performed on standard reference sources. In today's instrument the computation of complex spectra based on eq. 10 is not a burden anymore. Fast Fourier Transform algorithm (FFT) coupled to actual capabilities of small PC computer can deliver a high resolution spectrum almost in real time.

In summary, it is important to emphasize that a real instrument is characterized by its complex responsivity

$$\mathbf{K}(\nu) = K(\nu)\, e^{i\,\psi(\nu)} \qquad [11]$$

where K(ν) and ψ(ν) represent the module and the phase of the instrument responsivity **K**(ν). The bold face notation is used throughout this paper to identify complex numbers. The

remaining part of this document is mainly dedicated to the analysis of the instrument responsivity for different instrument configurations. In particular, the inter-relation between self IR emission, instrument responsivity and calibration is treated in view to find optimum configurations. In this context, a useful relation to compare one interferometer configuration with another is found by inserting eq. 11 into eq. 4, which gives

$$f(x) = K(\nu) \cos [2\pi\nu x + \psi(\nu)] \qquad [12]$$

where f(x) is the interferogram component corresponding to a single spectral element of a spectrally uniform source of unit intensity defined by a δ-Dirac i.e., $B(\nu) = \delta(\nu'-\nu)$ This is the relation used here as a reference for comparing the impact of internal component configurations on the interferometer responsivity.

2.2 Self-emission and Calibration of Standard FTIR Spectrometers

The schematic of the instrument shown in Fig. 1 corresponds to a standard single-input beam Michelson interferometer. For a real instrument of this type the output signal is actually composed of radiation from different origins. As it turns out, an important part of this radiation comes from the external source under study L. The remaining contributions are generated by the instrument itself. This parasite radiation is due to graybody emissions and stray light reflections from the interferometer components (lenses, mirrors, inner walls and others). It is referred to as the self-emission of the instrument. Figure 2 identifies the various sources of radiation intervening in a single measurement: L is the spectral radiance of the external source (target source), $\mathbf{SE}_{in}$ and $\mathbf{SE}_{out}$ represent the self-emissions (raw spectra) generated by the input and the output optics, respectively, and $\mathbf{SE}_{BS}$ represents the beamsplitter self-emission (raw spectrum). In the infrared the self-emission terms mainly depend on the temperature of the intervening components. It is quite significant especially for instrument operated at or near room temperature. Taken separately each of these radiation sources generates a specific interferogram and consequently a corresponding raw spectrum. The sum of these individual raw spectra is given by

$$\mathbf{S} = (\mathbf{K}\,\mathbf{L}) + \mathbf{SE}_{in} + \mathbf{SE}_{out} + \mathbf{SE}_{BS} \qquad [13]$$

which can be simplified by defining an instrument offset **O** such that

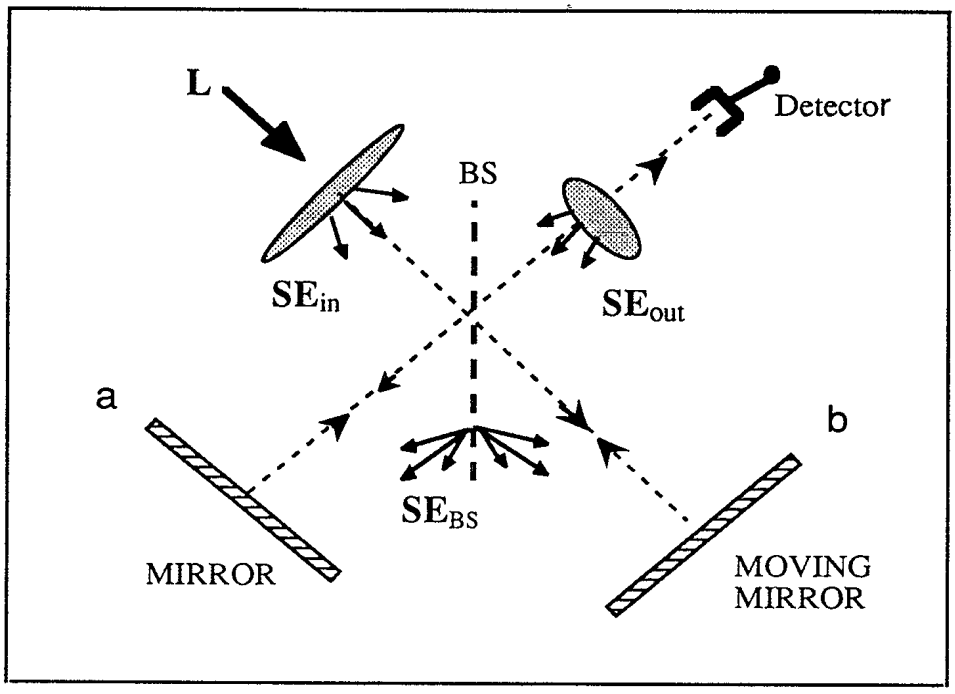

FIGURE 2 -Source and self-emission contributions from interferometer components. L is the spectral radiance of the external source, $\mathbf{SE}_{in}$ and $\mathbf{SE}_{out}$ represent the self-emission contributions from the input optics and the output optics, respectively, and $\mathbf{SE}_{BS}$ represents the beamsplitter self-emission contribution.

$$\mathbf{O} = \frac{1}{\mathbf{K}}(\mathbf{SE}_{in} + \mathbf{SE}_{out} + \mathbf{SE}_{BS}), \qquad [14]$$

yielding

$$\mathbf{S} = \mathbf{K}(\mathbf{L} + \mathbf{O}) \qquad [15]$$

Equation 15 represents the usual way to link the complex raw spectrum **S** to the target spectrum L (the one to be evaluated) taking into account the instrument characteristics which are the complex spectral responsivity **K** and the complex spectral offset **O**. As seen in eq. 14 the spectral offset of the instrument is a rather complicated expression involving three

different self-emission terms that are theoretically difficult to evaluate particularly for this type of instrument (single-beam).

Usually the self-emission terms are not stable in time due to thermal variations of instrument components. For this reason, the best way to acquire radiometrically accurate target spectra is by doing frequent calibration measurements. Ideally, this calibration is performed concurrently with each source measurement. The current method used for the accurate calibration (radiometric) of interferometric spectra is known as the two-temperature calibration method. The best variant of this method was proposed by Revercomb et al. (Ref. 7). In this method, two reference blackbodies of known radiances B_{hot} and B_{amb} are required to solve the two unknowns, the spectral responsivity and the spectral offset of the instrument. Often in FTIR work, the hot reference blackbody is kept at a constant temperature near 60° C and the second one is at ambient temperature near, 20° C. Defining the two corresponding raw spectra of reference as S_{hot} and S_{amb} then the solution of eq. 15 yields

$$\mathbf{K} = \frac{S_{hot} - S_{amb}}{B_{hot} - B_{amb}} \qquad [16]$$

and

$$\mathbf{O} = \frac{S_{amb}B_{hot} - S_{hot}B_{amb}}{S_{hot} - S_{amb}} \qquad [17]$$

And the calibrated target spectrum is obtain from

$$L = \frac{S}{K} - O \qquad [18]$$

The above discussion illustrates the usual limitation (radiometric calibration) encountered with most of standard FTIR instruments, i.e. the presence of variable and uncontrolled self-emissions, which necessitates three consecutive measurements (target and two references) for obtaining a single calibrated spectrum L. This represents a burden especially for real-time applications. In order to make the instrument more stable radiometrically and, consequently, more simple to calibrate we propose to exploit and optimize certain attributes of the double-input beam interferometer design. As seen below this type of interferometer is also suited for developing an FTIR spectrometer adapted for differential detection.

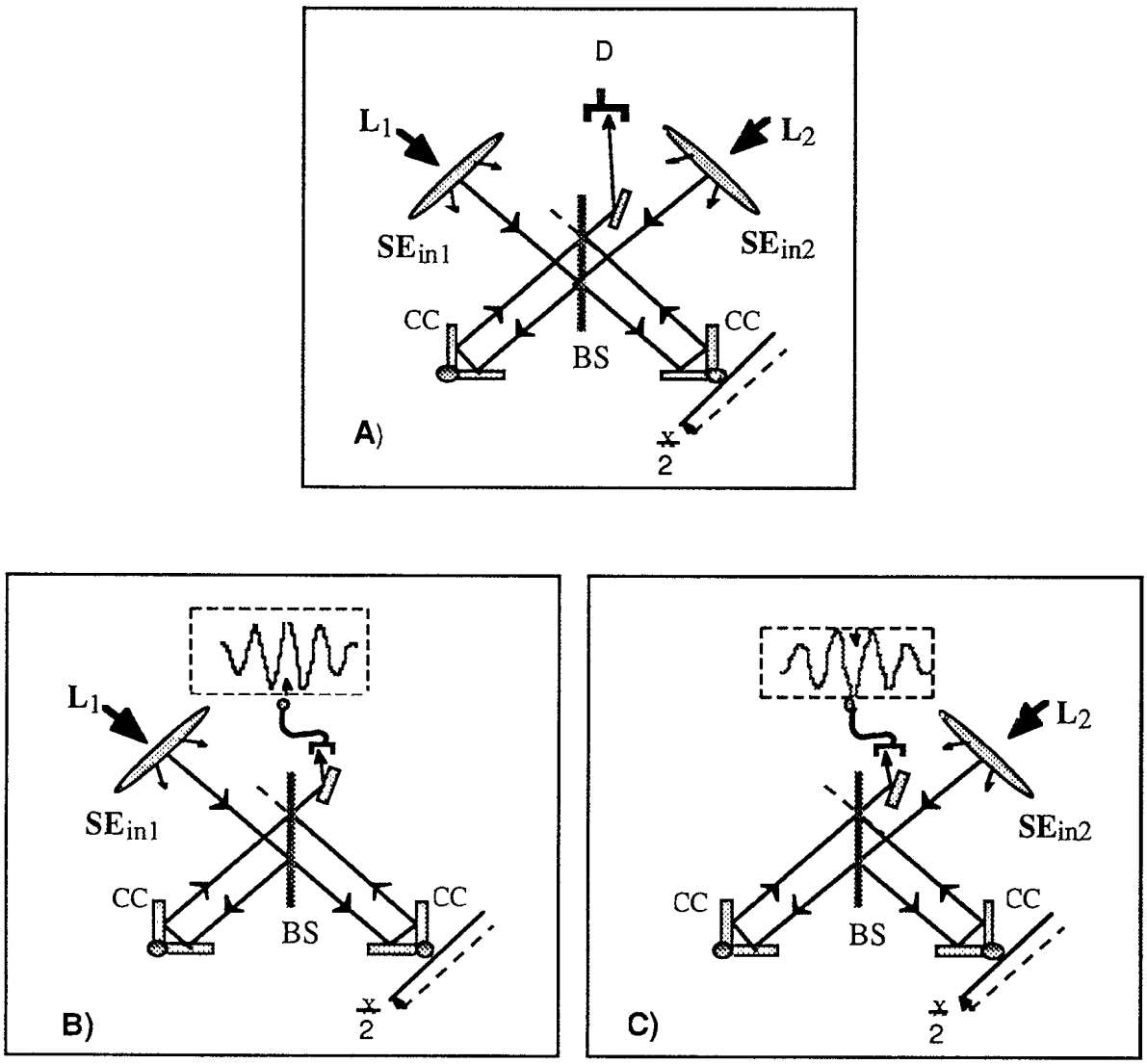

FIGURE 3 -Schematic view of a double-beam Michelson interferometer (a) that uses corner reflectors rather than standard flat plates. Figures b and c illustrate the two out-of-phase interferograms intervening in a double-beam interferometer (see text).

2.3 Double-input Beam Interferometer

Among the few numbers of double-beam interferometers, the modified Michelson with corner cube retroreflectors represents a good design to start with from the point of view of its optimization: self-emission suppression and simplified calibration. This is the basic design retained in our approach. Figure 3a represents a schematic view of the double-beam Michelson interferometer. The use of corner reflectors rather than standard flat plate mirrors has two main advantages for our application. First, the reflected beams from corner reflectors are offsetted laterally from the incident beams. This has the great advantage of decoupling input and output channels, as opposed to the standard single-beam interferometer (Fig. 2) where incident and reflected beams are superimposed. This attribute makes it possible to adjust independently the self-emission of each input ports without affecting in any way the output optics, which is not possible with the single-beam configuration. Note that the instrument also has a second output optics. For the sake of simplicity, the following analysis is restricted to only one of the two outputs but our conclusions apply equally to both in a straightforward manner. With this type of interferometer the two beams from the two inputs are optically combined in a subtractive manner. This optical subtraction arises from the fact that the two interferograms associated with each input port can be made out of phase, depending on the instrument design as discussed in the following section. Figures 3b and 3c illustrate the two out of phase interferograms intervening in this double-beam interferometer.

3.0 THE PROPOSED FTIR SPECTROMETER CONFIGURATION

The strategy behind the proposed FTIR spectrometer consists in designing a double-beam interferometer such that the two self-emission terms from each input ports fully cancels out by optical subtraction, i.e. when the two self-emission terms are equal in intensity and 180° out of phase leading to a theoretically perfect cancellation. To our knowledge, such a design to suppress the self-emission in FTIR spectrometer by optical subtraction has not been proposed in the past. This constitutes the basic effort of the present work: an FTIR spectrometer design which is optimized to suppress the internal self-emission by optical subtraction using a properly balanced dual-beam interferometer.

The proposed design is the result of a previous investigation on the subtraction performance of a commercial dual-beam interferometer, the MB-100 manufactured by Bomem. Although the MB-100 was not specifically optimized for optical subtraction, its utilization provided a good understanding of the basic principles. From that investigation it

appeared that there are two main factors limiting the accuracy of the subtraction. The first limiting factor is related to the optical configuration of the two input ports (mirrors and windows). These two inputs must be as symmetric as possible to ensure the same beam attenuation and consequently the same emissions from both ports. For instance if the absorption of a mirror (or lens) from input-1 is higher than its counterpart from input-2, then the resulting unbalance corresponds to a larger emission from input-1. In practice, it is relatively easy to satisfy this symmetry requirement with a proper mechanical design and the use of identical optical components in each input port.

The second limiting factor is related to the IR absorption and, consequently, the self-emission of the beamsplitter. Of the two limiting factors the beamsplitter one is the most important. For this reason, the remaining part of this report mainly focus on the beamsplitter issue assuming that the two input ports of the double-beam interferometer are symmetric.

More formally, the following equations serve to establish the expected attributes of the optimized instrument. For an FTIR spectrometer based on a double-input port interferometer the total signal **S** represents the sum of two individual complex raw spectra, $\mathbf{E}_1$ and $\mathbf{E}_2$, associated with each inputs. If input-1 and input-2 aim at target sources of radiance L_1 and L_2, respectively, the resulting raw spectrum is given by (see Fig. 3a)

$$\mathbf{S} = \mathbf{E}_1 + \mathbf{E}_2 + \mathbf{E}_{BS} \qquad [19]$$

with

$$\mathbf{E}_1 = \mathbf{K}_1 (L_1 + \mathbf{S}\mathbf{E}_{in1}) \qquad [20]$$

$$\mathbf{E}_2 = \mathbf{K}_2 (L_2 + \mathbf{S}\mathbf{E}_{in2}) \qquad [21]$$

where $\mathbf{K}_1$, $\mathbf{K}_2$ and $\mathbf{SE}_{in1}$, $\mathbf{SE}_{in2}$ are defined as the responsivities and the self-emissions associated with input-1 and input-2, respectively, and $\mathbf{E}_{BS}$ represents the self-emission from the beam splitter. Note that by comparison to the source radiance terms L_1 and L_2, the self-emission terms may have a phase delay because they may originate from different location. To study the radiometric symmetry or balance of the dual-beam interferometer it is advantageous to proceed by analogy with the single-beam calibration approach (eqs. 16-18). In the particular case where the calibration is performed on input-1 while source L_2 is fixed for the three measurements (target and two references) then the corresponding raw spectrum can be written as

$$\mathbf{S} = \mathbf{K}_1 (L_1 + \mathbf{O}_1) \qquad [22]$$

with

$$\mathbf{O}_1 = \left(\mathbf{SE}_{in1} + \frac{\mathbf{K}_2}{\mathbf{K}_1} L_2 + \frac{\mathbf{K}_2}{\mathbf{K}_1} \mathbf{SE}_{in2} + \frac{\mathbf{E}_{BS}}{\mathbf{K}_1} \right). \qquad [23]$$

In this case the source L_2 acts a part of the instrument offset. Equations 22 and 23 link the complex raw spectrum $\mathbf{S}$ to the target spectrum L_1 (the one to be evaluated) taking into account the characteristics of the double-beam interferometer which are the complex spectral responsivity $\mathbf{K}_1$ and the complex spectral offset $\mathbf{O}_1$ associated to channel-1.

Alternatively, if the calibration is performed on input-2 while the source L_1 is fixed for the three measurements, then the corresponding raw spectrum can be written as

$$\mathbf{S} = \mathbf{K}_2 (L_2 + \mathbf{O}_2) \qquad [24]$$

with

$$\mathbf{O}_2 = \left(\mathbf{SE}_{in2} + \frac{\mathbf{K}_1}{\mathbf{K}_2} L_1 + \frac{\mathbf{K}_1}{\mathbf{K}_2} \mathbf{SE}_{in1} + \frac{\mathbf{E}_{BS}}{\mathbf{K}_2} \right). \qquad [25]$$

In this case source L_1 acts as a part of the instrument offset. Equations 24 and 25 link the complex raw spectrum $\mathbf{S}$ to the target spectrum L_2, taking into account the characteristics of the double-beam interferometer which are the complex spectral responsivity $\mathbf{K}_2$ and the complex spectral offset $\mathbf{O}_2$ associated to channel-2.

From equations 23 and 25 it can be seen that the spectral offsets $\mathbf{O}_1$ and $\mathbf{O}_2$ which represent the self-emission contributions associated with channel-1 and channel-2, respectively, can be minimized by the fulfillment of the three following conditions:

CONDITION-1: Balanced responsivities,

$$\mathbf{K}_1 = -\mathbf{K}_2 = \mathbf{K}_2 e^{i\pi} \qquad [26]$$

CONDITION-2: Balanced emissions,

$$\mathbf{SE}_{in1} = \mathbf{SE}_{in2} \qquad [27]$$

CONDITION-3: Beamsplitter transparency

$$\mathbf{E}_{BS} = 0 \qquad [28]$$

By application of these three conditions, the resulting raw spectrum derived from eqs. 22 to 25 reduces to

$$\mathbf{S} = \mathbf{K}_1 (L_1 - L_2) . \qquad [29]$$

Equations 26 to 28 define in a mathematical sense the conditions for an optimized FTIR spectrometer as proposed in the present work. As seen, eq. 29 does not contain any self-emission terms from the instrument itself. The resulting raw spectrum **S** is directly proportional to the difference between the two source radiances $L_1 - L_2$. Consequently, for single-beam operations this instrument requires the use of a fixed reference source of known radiance ($L_{ref} = L_2$) attached to the second input port. This reference can be a simple flat plate blackbody (Fig. 4) having a thermocouple for monitoring the plate temperature (T_{ref}), which allows the computation of the Planck radiance $L(T_{ref})$. In this case, the calibrated spectrum L_1 is directly given by

$$L_1 = \left(\frac{\mathbf{S}}{\mathbf{K}_1} + L(T_{ref}) \right) . \qquad [30]$$

There are several advantages associated with this approach. First, it considerably simplifies the radiometric calibration where in principle only one reference measurement is needed to evaluate solely the spectral responsivity $\mathbf{K}_1$ of the instrument (no offset). Moreover, because the responsivity can be correlated empirically to the beamsplitter temperature (T_{BS}) then the calibrated spectrum can be generated in real time directly from the monitored beamsplitter temperature and using pre-stored responsivity coefficients to generate $\mathbf{K}_1(T_{BS})$ in real time. In these conditions, the calibrated radiance becomes

$$L_1 = \left(\frac{\mathbf{S}}{\mathbf{K}_1(T_{BS})} + L(T_{ref}) \right) . \qquad [31]$$

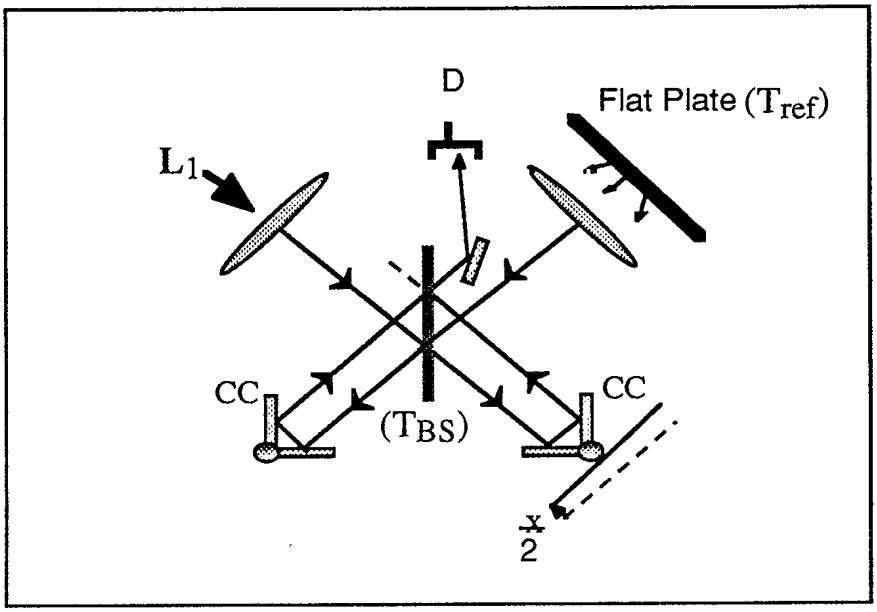

FIGURE 4 - Optical configuration for single beam measurements with the optimized FTIR spectrometer: a flat plate

The net result of the proposed design is an FTIR spectrometer that requires only the monitoring of instrument temperatures (beamsplitter and flat plate) to generate, in real time, a calibrated spectrum according to eq. 31. This represents a definite advantage over the existing FTIR spectrometers that use three spectral measurements (source and two references) to generate the calibrated spectrum. In practical design, the casing of the instrument can be made to integrate the flat plate and the beamsplitter onto the same mount such that $T_{BS} = T_{ref}$ resulting in only one temperature monitoring to obtain the calibrated spectrum, i.e.

$$L_1 = \left(\frac{S}{K_1(T_{BS})} + L(T_{BS}) \right). \qquad [32]$$

A final advantage of the proposed design is for differential detection (using both inputs as shown in Fig. 3a) of weak IR signatures against large spectral background. Because the subtraction is instantaneously performed optically, the resulting background-free spectrum benefits from the full range of signal amplification as opposed to sequential subtraction

technique where the range of signal amplification is mainly limited by the background itself. In this case, the calibrated radiance differential can be evaluated in real time using

$$\delta L = \frac{S}{K_1(T_{BS})} \qquad [33]$$

where $\delta L = L_1 - L_2$. More information concerning the differential detection of chemical vapors using a double-beam FTIR interferometer can be found in a recent paper (Ref. 5).

The conditions discussed above to obtain an optimized FTIR spectrometer impose two basic requirements on the instrument design. The first requirement implies that the transmissions, the absorptions and the corresponding self-emissions produced by the components of the two input ports, including mirrors, lens, attenuators and masks must be symmetrically the same to satisfy CONDITIONS-1 and 2 (eq. 26-27). This can be achieved in a straightforward manner using simple symmetry considerations such that one half of the instrument (and input components) can be considered as the mirror reflection of the other half taking the beamsplitter plan as reference. It is important to note that the thermal properties of the instrument must also satisfy the same symmetry arguments to ensure that the temperature and consequently the graybody emission of intervening components of each input port are symmetrically the same.

The second requirement is related to the beamsplitter itself. In this case, the design of a beamsplitter that satisfies the three conditions of optimization (see eqs. 26-28) cannot be stated simply. In the next chapter we present an analytical development which provides a tool for designing the beamsplitter. We also propose an optimized beamsplitter configuration.

4.0 BEAMSPLITTER CONFIGURATIONS: ANALYTICAL DEVELOPMENT

In the following, the basic theory of optical interference is used to specify the attributes of different beamsplitter configurations. This analytical development begins with a review on some current beamsplitter configurations that do not match the optimization conditions (eqs. 26-28) followed by the treatment of two cases having a suitable beamsplitter configurations. The first case corresponds to a beamsplitter made of an optically thin layer of a material. Self-supported thin films of gold, germanium and diamond are among this category. It is shown that this configuration (thin layer) adequately balances the two responsivities, but it has

the drawback of generating unwanted self-emissions when the layer is absorbing. The second case corresponds to a beamsplitter made of an optically thin layer of air squeezed between two thick substrates properly covered with antireflection coatings on their external faces. It has been shown that this beamsplitter configuration can fully satisfy the three conditions for achieving an optimized FTIR spectrometer: balanced responsivities, balanced emissions and layer transparency. This is the configuration proposed in the present work as a claim for the optimized FTIR spectrometer. In the following, the basic theory of optical interference is used to specify the attributes of different beamsplitter configurations. This analytical development begins with a review on some current beamsplitter configurations that do not match the optimization conditions (eqs. 26-28).

4.1 Unsuitable Beamsplitter Configurations

One of the most simple beamsplitter assembly used in interferometers is made of a single substrate with or without coatings on its interfaces. Figure 5 illustrates the ray tracing inside a double-beam interferometer that makes use of such a beamsplitter. It is easily seen that the interfering rays from input-1 (Fig. 5a) propagate only once into the substrate, while the interfering rays from input-2 (Fig. 5b) propagate twice. Consequently, this beamsplitter configuration generates a permanent unbalance equal to T_S (substrate transmittance) between the two responsivities associated to each input. In this case, the only way to satisfy the condition-1 of optimization (eq. 26) is by restricting the spectral band of operation to a region where the substrate material is perfectly transparent. This represents a major constraint because most of the usual substrates used in infrared, such as germanium and zinc selenide, exhibit absorption in certain parts of the spectrum. This limitation makes this type of beamsplitter unsuitable for the design of an optimized FTIR spectrometer. Another single substrate configuration developed specifically for double-beam interferometers with corner cube reflectors is shown in Fig. 6. The main difference with the above mentioned configuration is that the number of interaction (transmission and reflection) of interfering rays with the substrate coatings is reduced, which minimizes losses and increases the sensitivity of the instrument. However the ray tracings show the same limitation as for the preceding configuration. Interfering rays from input-1 (Fig. 6a) propagate only once into the substrate while interfering rays from input-2 (Fig. 6b) propagate twice generating the same permanent unbalance (T_S) which is not suitable for the design of an optimized FTIR spectrometer.

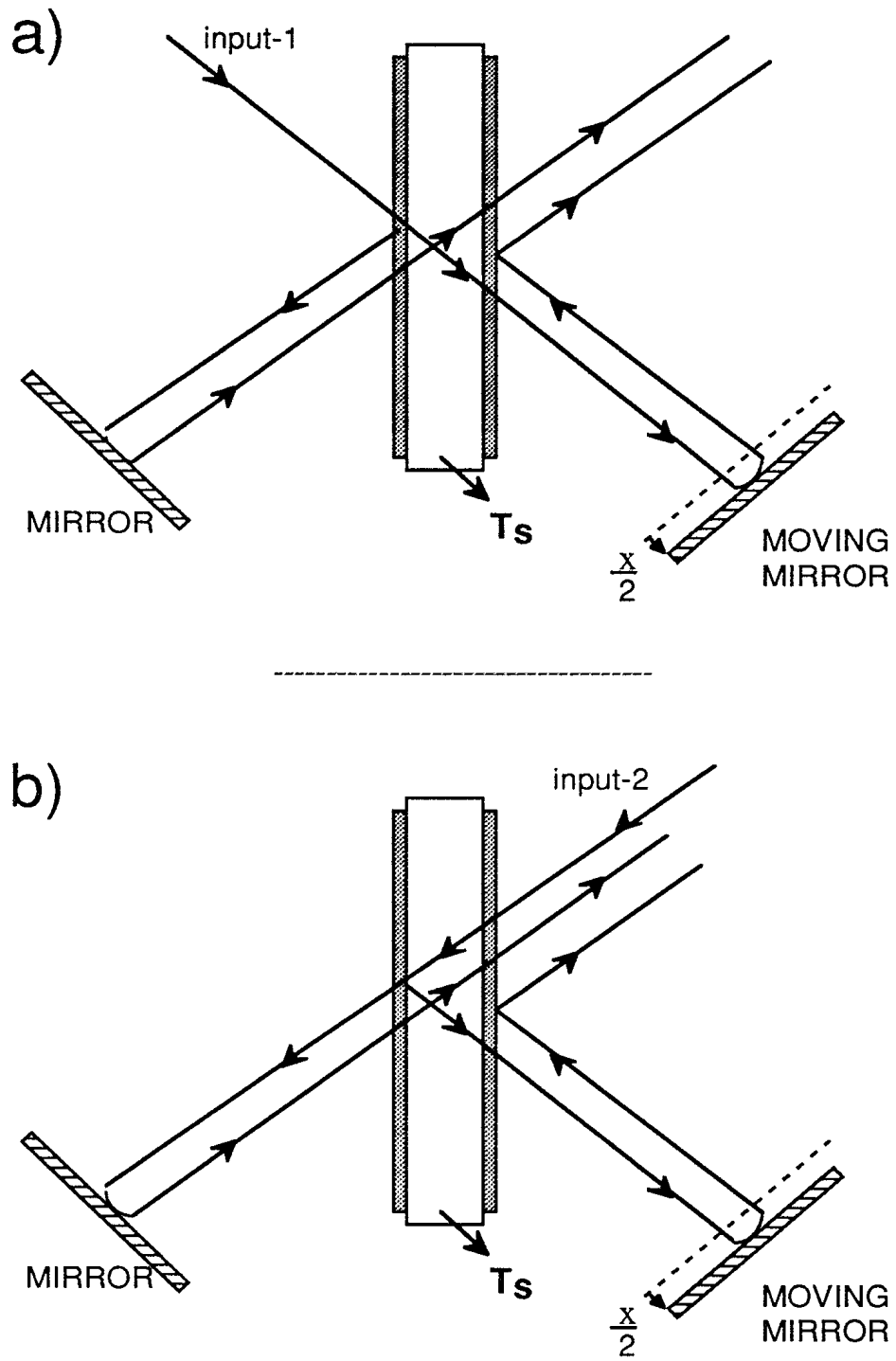

FIGURE 5 - Ray tracing for a beamsplitter made of a coated substrate: a- the interfering rays from input-1 propagate only once into the substrate, and b- the interfering rays from input-2 propagate twice into the substrate

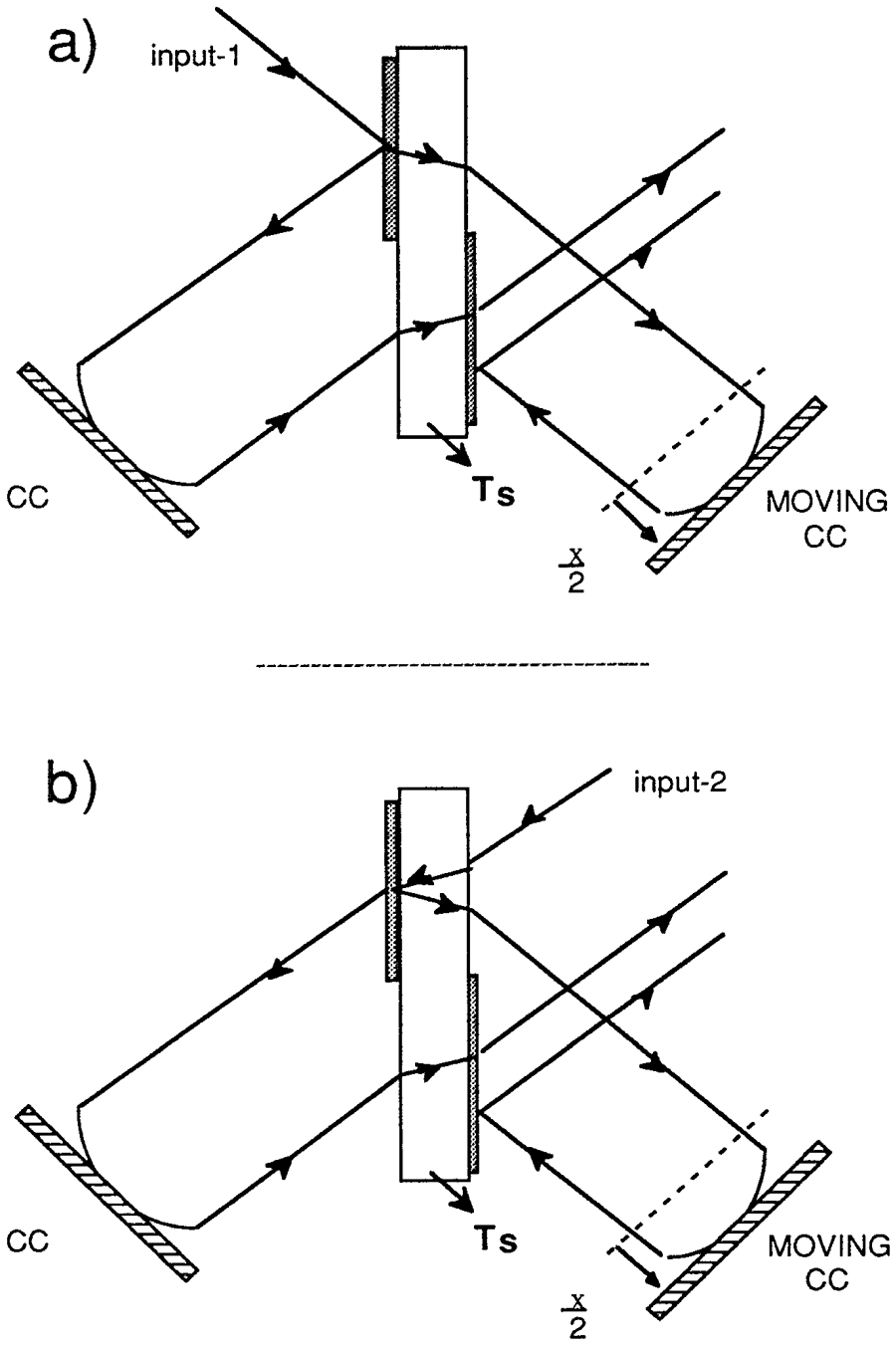

FIGURE 6 - Ray tracing for a single half-coated substrate: a- the interfering rays from input-1 propagate only once into the substrate, and b- the interfering rays from input-2 propagate twice into the substrate

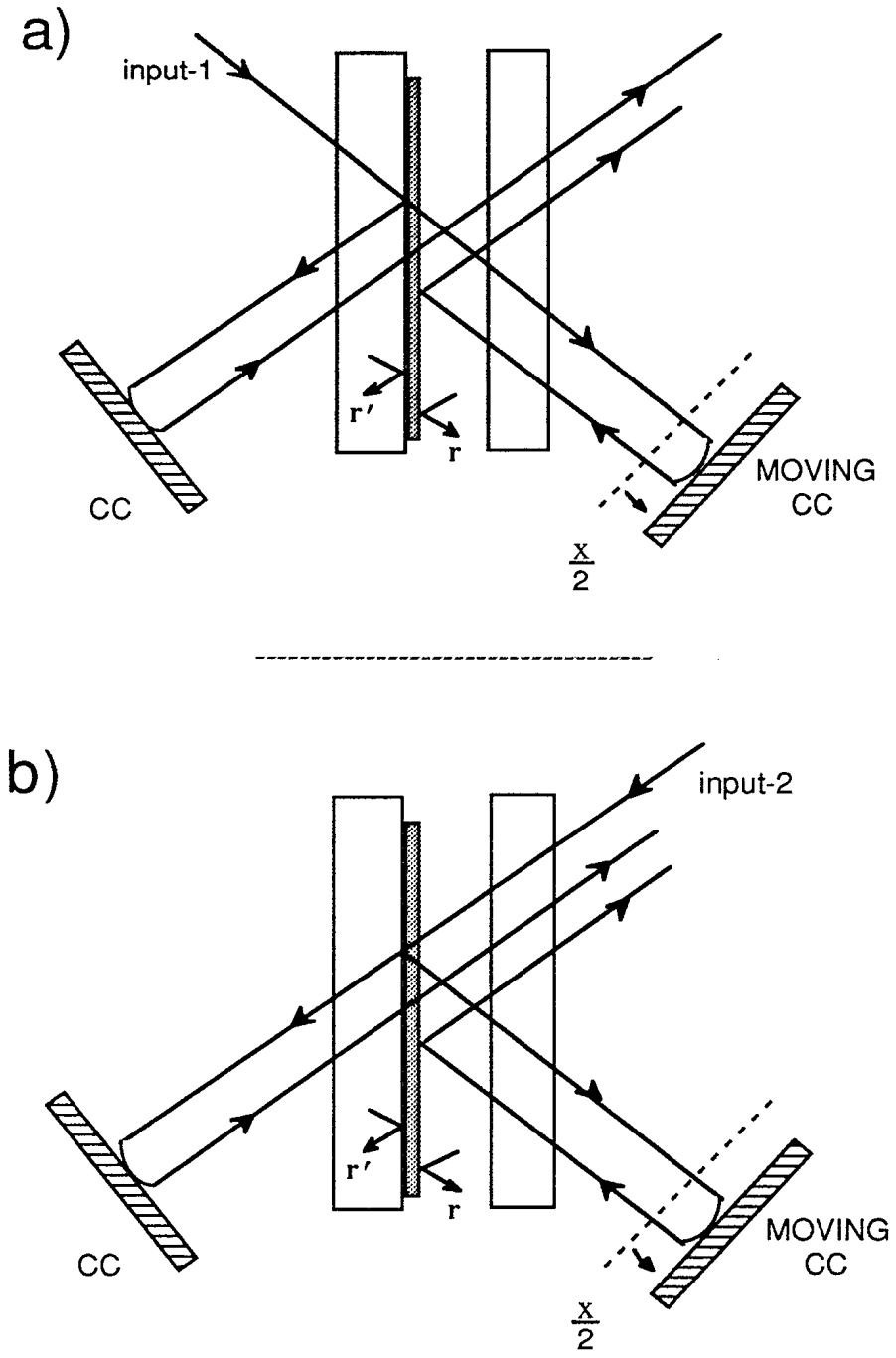

FIGURE 7 - Ray tracing for a beamsplitter assembly made of a single-side coated substrate with a compensating plate (substrate). a- A part of the radiation from input-1 exhibits a substrate-layer reflection (**r'**) and, b- for input-2 the radiation exhibits only air-layer reflections (**r**).

A more symmetrical beamsplitter configuration is shown in Fig. 7 where a splitting coating is present on the inner face of a first substrate and a second one is added as a compensating plate. In this case, the number of passes through the substrates is identical for both rays from input-1 and input-2. However, this configuration exhibits another source of dissymmetry which comes from the coating itself. As seen by comparing Figs. 7a and 7b, a part of the radiation from input-1 exhibits a substrate-layer reflection (**r'**), while for input-2 the radiation exhibits only air-layer reflections (**r**). It can be shown, from optical thin film theory, that the two reflection coefficients **r** and **r'** are not identical when the coating is absorbing. This has for consequence to unbalance the responsivities and the self-emissions between the two inputs in spectral regions where the splitting coating is absorbing. Unfortunately, most of the coatings actually used for IR beamsplitters may absorb in certain infrared regions. For instance, germanium and thorium fluoride coatings absorb in the far IR. Consequently, this beamsplitter configuration and, by extension, any other configurations which do not match the number of **r** and **r'** reflections between input-1 and input-2 do not appear suited for an optimized FTIR spectrometer. This suggests the use of a fully symmetrical beamsplitter in which **r'** = **r** and where the number of passes through the substrates are equivalently the same for input-1 and input-2. This is the strategy proposed in the next sections.

4.2 Thin Layer Beamsplitter

The theory of optical interferences is used to establish the responsivities $\mathbf{K}_1$ and $\mathbf{K}_2$ of a double-beam interferometer-spectrometer having a thin layer beamsplitter. In this case, the ray tracings in Figs. 8a and 8b indicate that the output amplitudes ($\mathbf{A}_1$ and $\mathbf{A}_2$) for beams of unit amplitudes incident on input-1 and input-2 are given by

$$\mathbf{A}_1 = \mathbf{r}\,\mathbf{t} + \mathbf{t}\,\mathbf{r}\,e^{i\phi}\,, \qquad [34]$$

$$\mathbf{A}_2 = \mathbf{r}\,\mathbf{r} + \mathbf{t}\,\mathbf{t}\,e^{i\phi}\,, \qquad [35]$$

where **r** and **t** represent the amplitude reflection and transmission of the layer and

$$\phi = 2\pi\nu x \qquad [36]$$

expresses the phase difference between the two interfering beams in terms of the optical path difference x (see Fig. 8a). Following Heavens (Ref. 8), the amplitude reflection and transmission of the layer can be explicitly evaluated by summing the contributions from multiple reflections and transmissions inside the layer. For a layer symmetrically bounded by identical media, such as in Fig. 8c, the summations yield

$$\mathbf{r} = \frac{r_1 \left(1 - e^{-2i\delta}\right)}{1 - r_1^2 e^{-2i\delta}} \qquad [37]$$

$$\mathbf{t} = \frac{\left(1 - r_1^2\right) e^{-i\delta}}{1 - r_1^2 e^{-2i\delta}} \qquad [38]$$

with

$$\delta = 2\pi\nu nd \cos(\theta) \qquad [39]$$

where δ is the phase shift due to a layer of optical thickness nd, n is the refractive index of the layer and θ is the angle of refraction inside the material.. Equations 37 and 38 are obtained using the following identities (Heavens, Ref. 8, p. 51- 57) between Fresnel coefficients associated to the interfaces of the layer

$$r'_1 = - r_1 \qquad [40]$$

$$t'_1 \, t_1 = \left(1 - r_1^2\right). \qquad [41]$$

Equating the denominators of eqs. 37 and 38 leads to a simple expression connecting the amplitude reflection and transmission such that

$$\mathbf{t} = \mathbf{r}\, H\, e^{-i\frac{\pi}{2}} \qquad [42]$$

where H is an intermediate variable defined as

$$H = \frac{\left(1 - r_1^2\right)}{2\, r_1 \sin(\delta)}. \qquad [43]$$

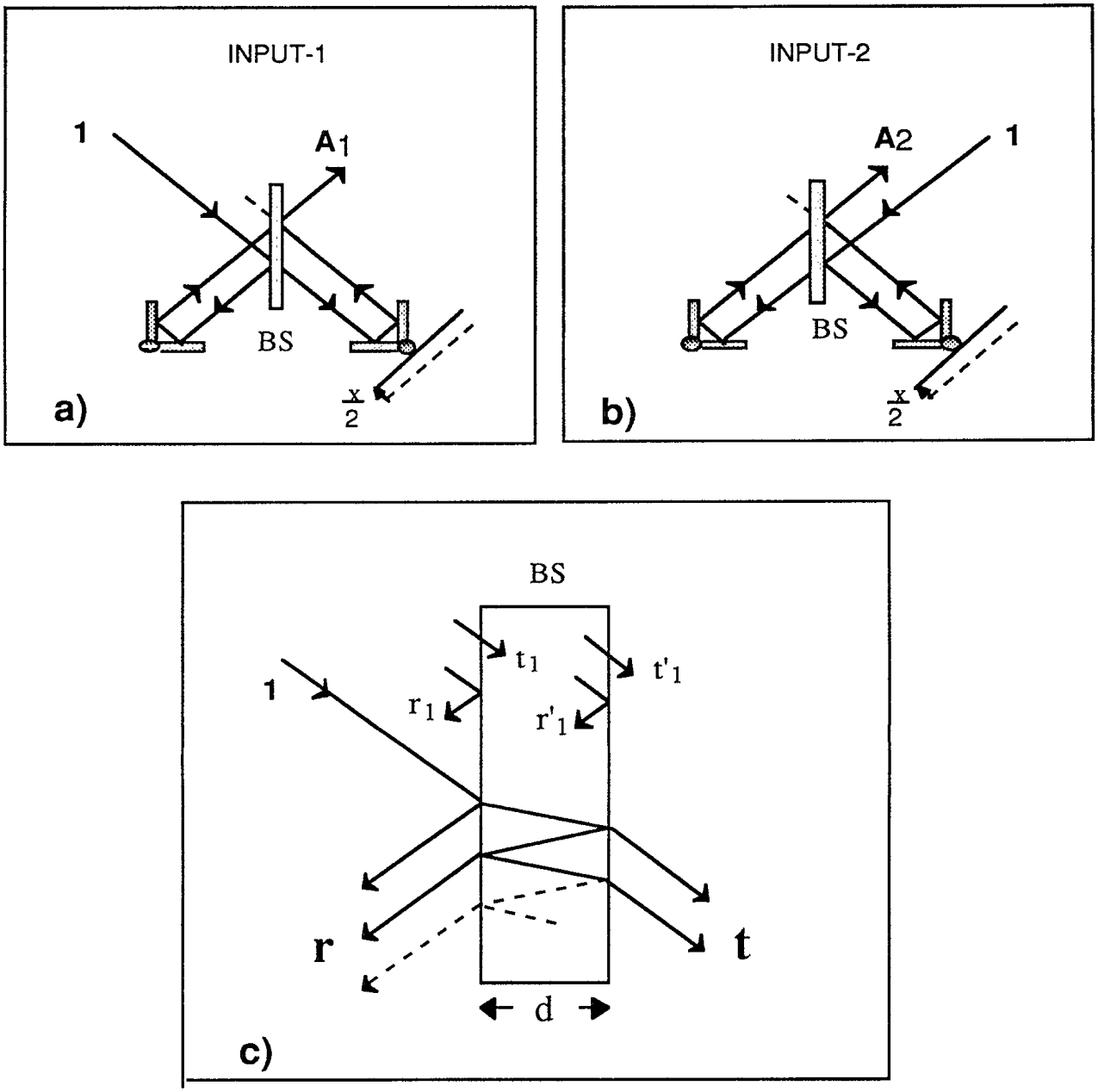

FIGURE 8 - Ray tracings showing the output amplitudes (A_1 and A_2) for beams of unit amplitude incident on input-1 (a) and input-2 (b) and the amplitude reflection and transmission (c) of a thin layer beamsplitter

Equations 42 and 43 are useful relations which simplify the analysis for obtaining the responsivities of the interferometer.

Coming back to eqs. 34 and 35 and multiplying the two output amplitudes by their complex conjugates ($\mathbf{A^*}_1$ and $\mathbf{A^*}_2$) yields the two output intensities I_1 and I_2 associated with each input port, i.e.

$$I_1 = \mathbf{A}_1\ \mathbf{A^*}_1 = \left(\mathbf{r}\,t + t\,\mathbf{r}\,e^{i\phi}\right)\left(\mathbf{r^*}\,t^* + t^*\,\mathbf{r^*}\,e^{-i\phi}\right), \qquad [44]$$

$$I_2 = \mathbf{A}_2\ \mathbf{A^*}_2 = \left(\mathbf{r}^2 + t^2\,e^{i\phi}\right)\left(\mathbf{r^*}^2 + t^{*2}\,e^{-i\phi}\right). \qquad [45]$$

Taking the coefficient of reflection in intensity of the layer $R = \mathbf{r}\,\mathbf{r^*}$ and inserting eq. 42 into the two preceding equations yield for the two output intensities

$$I_1 = \left(2\,R^2\,H^2 + 2\,R^2\,H^2\cos(\phi)\right) \qquad [46]$$

$$I_2 = \left(R^2 + R^2\,H^2 + 2\,R^2\,H^2\cos(\phi - \pi)\right). \qquad [47]$$

In eqs. 46 and 47 the modulated components of intensities represent the interferograms associated with each input port. It follows that the two responsivities $\mathbf{K}_1$ and $\mathbf{K}_2$ associated with each inputs are given by

$$\mathbf{K}_1 = 2\,R^2\,H^2, \qquad [48]$$

$$\mathbf{K}_2 = -\,2\,R^2\,H^2. \qquad [49]$$

which satisfies the CONDITION - 1 (eq. 26) of balanced responsivities where

$$\mathbf{K}_1 = -\,\mathbf{K}_2. \qquad [50]$$

Although this simple configuration satisfies the balanced responsivities condition, it is shown below that such a self-supported layer can generate unwanted self-emission when the layer is absorbing (Section 4.5).

4.3 Proposed BS Configuration: Responsivity Evaluations

This configuration corresponds to a beamsplitter (BS) made of an optically thin layer of air squeezed between two thick substrates properly covered with antireflection coatings on their external faces. Again, the goal is to establish the responsivities $\mathbf{K}_1$ and $\mathbf{K}_2$ of the double-beam interferometer-spectrometer with this beamsplitter configuration. For the moment, we will assume that the two substrates and their antireflection coatings may be optically different to simulate a possible mismatch. The ray tracings in Figs. 9a and 9b indicate that the output amplitudes ($\mathbf{A}_1$ and $\mathbf{A}_2$) for beams of unit amplitudes incident on input-1 and input-2 are given by

$$\mathbf{A}_1 = \left(t_{c1}^3 t_{s1}^3 \, r \, t \, t_{c2} \, t_{s2} \right) + \left(t_{c1} \, t_{s1} \, t \, r \, t_{c2}^3 \, t_{s2}^3 \, e^{i\phi} \right) \qquad [51]$$

and

$$\mathbf{A}_2 = \left(t_{c2}^2 \, t_{s2}^2 \, t^2 \, t_{c1}^2 \, t_{s1}^2 \right) + \left(t_{c2}^4 \, t_{s2}^4 \, r^2 \, e^{i\phi} \right) \qquad [52]$$

where r and t represent the amplitude reflection and transmission of the thin air layer and ϕ (eq. 36) is the phase difference between the two interfering beams. Variables t_{c1}, t_{c2} and t_{s1}, t_{s2} are the amplitude transmissions (Fig. 9a) of the two antireflection coatings and the two substrates, respectively. To simplify the analysis it is convenient to express these amplitudes in terms of their respective modules and phases yielding

$$\begin{aligned} t_{s1} &= t_{s1} \, e^{i\sigma_1} \\ t_{s2} &= t_{s2} \, e^{i\sigma_2} \\ t_{c1} &= t_{c1} \, e^{i\Gamma_1} \\ t_{c2} &= t_{c2} \, e^{i\Gamma_2} \end{aligned} \quad . \qquad [53]$$

Using these expressions into eqs. 51 and 52 leads to after rearrangements

$$\mathbf{A}_1 = t_{c1} \, t_{s1} \, r \, t \, t_{s2} \, t_{c2} \left[t_{s1}^2 \, t_{c1}^2 \, e^{i(2\sigma_1 + 2\Gamma_1)} + t_{s2}^2 \, t_{c2}^2 \, e^{i(2\sigma_2 + 2\Gamma_2)} \, e^{i\phi} \right] \qquad [54]$$

and

$$\mathbf{A}_2 = t_{c2}^2\, t_{s2}^2 \left[t^2\, t_{s1}^2\, t_{c1}^2\, e^{\,i\,(2\sigma_1 + 2\Gamma_1)} + r^2\, t_{s2}^2\, t_{c2}^2\, e^{\,i\,(2\sigma_2 + 2\Gamma_2)}\, e^{\,i\,\phi} \right] . \qquad [55]$$

The two output intensities I_1 and I_2 associated with each input port are found by multiplying the two output amplitudes by their complex conjugates ($\mathbf{A}^*_1$ and $\mathbf{A}^*_2$), which gives

$$I_1 = \mathbf{A}_1\, \mathbf{A}^*_1 = T_{c1} T_{s1}\, R^2\, T_{s2} T_{c2} \left[H^2\, T_{s1}^2 T_{c1}^2 + H^2\, T_{s2}^2 T_{c2}^2 + H^2\, T_{s1} T_{c1} T_{s2} T_{c2} \cos\,(\phi + \psi) \right]$$

[56]

and

$$I_2 = \mathbf{A}_2\, \mathbf{A}^*_2 = R^2\, T_{s2}^2\, T_{c2}^2 \left[H^4\, T_{s1}^2\, T_{c1}^2 + T_{s2}^2\, T_{c2}^2 + H^2\, T_{s1}\, T_{c1}\, T_{s2}\, T_{c2} \cos\,(\phi + \psi - \pi) \right]$$

[57]

where a phase offset due to an imperfect compensation of the interferometer has been defined as

$$\psi = 2\,(\sigma_2 + \Gamma_2 - \sigma_1 - \Gamma_1) \qquad [58]$$

and other quantities in capital letters are defined as follows

$R = r\, r^*$; Reflection in intensity of the thin layer of air,
$T_{s1} = t_{s1}\, t^*_{s1}$; Transmission in intensity of substrate-1,
$T_{c1} = t_{c1}\, t^*_{c1}$; Transmission in intensity of the antireflection coating onto substrate-1,
$T_{s2} = t_{s2}\, t^*_{s2}$; Transmission in intensity of substrate-2,
$T_{c2} = t_{c2}\, t^*_{c2}$; Transmission in intensity of the antireflection coating onto substrate-2,
and H is defined by eq. 43.

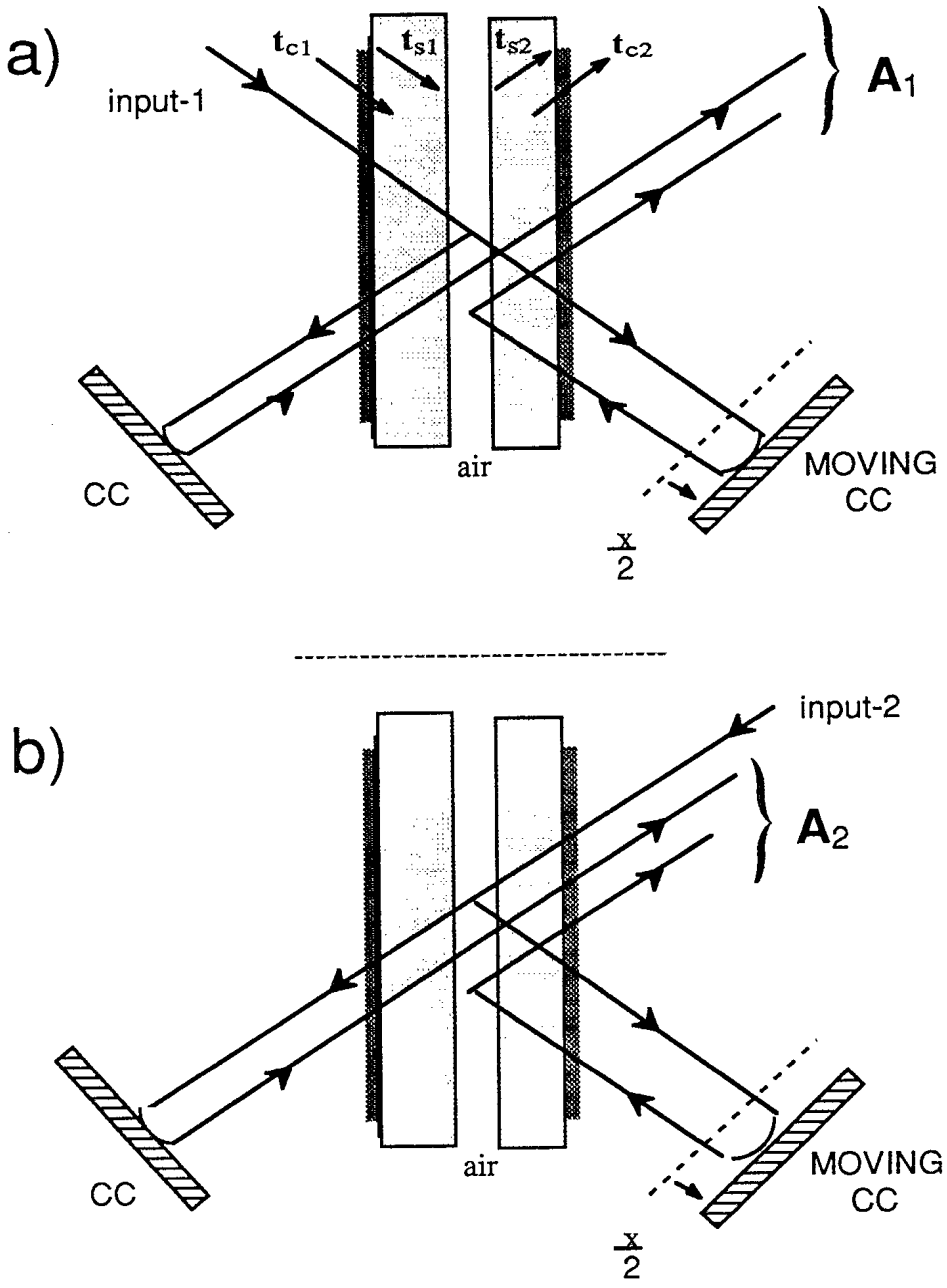

FIGURE 9 - Ray tracings showing the output amplitudes (A_1 and A_2) for beams of unit amplitudes incident on input-1 (a) and input-2 (b) for a beamsplitter made of an optically thin layer of air squeezed between two substrates properly covered with antireflection coatings on their external faces

Note that in eqs. 56 and 57 the transmission in intensity of the thin layer of air does not appear explicitly but is defined as $T = R\,H^2$, which is consistent with eq. 42 connecting the reflection and transmission coefficients of a thin layer.

Finally, in eqs. 56 and 57 the modulated components of the intensities represent the interferograms associated with each input ports. It follows that the two complex responsivities $\mathbf{K}_1$ and $\mathbf{K}_2$ associated with each input are given by

$$\mathbf{K}_1 = K_1\, e^{i\psi} = + R^2 H^2\, T_{s1}^2\, T_{c1}^2\, T_{s2}^2\, T_{c2}^2\, e^{i\psi} \qquad [59]$$

and

$$\mathbf{K}_2 = K_2\, e^{i\psi} = -\, R^2\, H^2\, T_{s1}\, T_{c1}\, T_{s2}^3\, T_{c2}^3\, e^{i\psi} \qquad [60]$$

which satisfies the balanced responsivities CONDITION - 1 (eq. 26) only when the two substrates and their antireflection coatings are optically identical i.e.

if

$$T_{s1} = T_{s2}\,, \qquad [61]$$

$$T_{c1} = T_{c2}\,, \qquad [62]$$

then

$$\mathbf{K}_1 = -\,\mathbf{K}_2 = R^2\, H^2\, T_{s1}^4\, T_{c1}^4\, e^{i\psi}\,. \qquad [63]$$

As will be seen further, the equations developed in this section will appear useful in the analysis of experimental results obtained with a prototype instrument designed with this type of beamsplitter.

4.4 Proposed BS configuration: Emission of substrates

The goal of this section is to show that the two emission components from each substrate composing the proposed beamsplitter configuration cancels out . First, it is assumed that both substrates may be absorbing and that their temperatures are identical yielding a

corresponding blackbody radiance equal to B_S. Using the parameters defined in Figs. 9a and 10, it is defined that

$$\varepsilon_1 = (1 - T_{c1}\, T_{s1})\; B_s \qquad [64]$$

where ε_1 represents the emission component from substrate-1 which is incident on the air layer. Other quantities has been defined in the previous section. Note that, in eq. 64, if both transmissions in intensity T_{c1} (AR coating) and T_{s1} (bulk substrate) are equal to one then the emission term vanishes. Following a ray tracing and a mathematical development similar to the one found in the previous section, it can be shown that the modulated component of the interferogram associated with this substrate emission is given by

$$\text{MODULATION}(\varepsilon_1) = [\,(1 - T_{c1}\, T_{s1})\, B_s\,]\;\; R^2\, H^2\, T_{s1}\, T_{c1}\, T_{s2}^2\, T_{c2}^2 \cos(\phi + \psi) \qquad [65a]$$

or equivalently in the spectral domain, the corresponding raw spectrum associated with substrate-1 emission is given by

$$\text{RAW SPEC}(\varepsilon_1) = \mathbf{K}_1 \frac{(1 - T_{c1}\, T_{s1})}{T_{c1}\, T_{s1}} B_s \qquad [65b]$$

where the complex responsivity $\mathbf{K}_1$ defined at eq. 59 has been introduced in the previous expression.

Similarly the emission component from substrate-2, which is incident on the air layer is defined as

$$\varepsilon_2 = (1 - T_{c2}\, T_{s2})\; B_s \qquad [66]$$

and the modulated component corresponding to substrate-2 emission is

$$\text{MODULATION}(\varepsilon_2) = [\,(1 - T_{c2}\, T_{s2})\, B_s\,]\;\; R^2\, H^2\, T_{s1}\, T_{c1}\, T_{s2}^2\, T_{c2}^2 \cos(\phi + \psi - \pi) \qquad [67a]$$

or equivalently the corresponding raw spectrum emission is given by

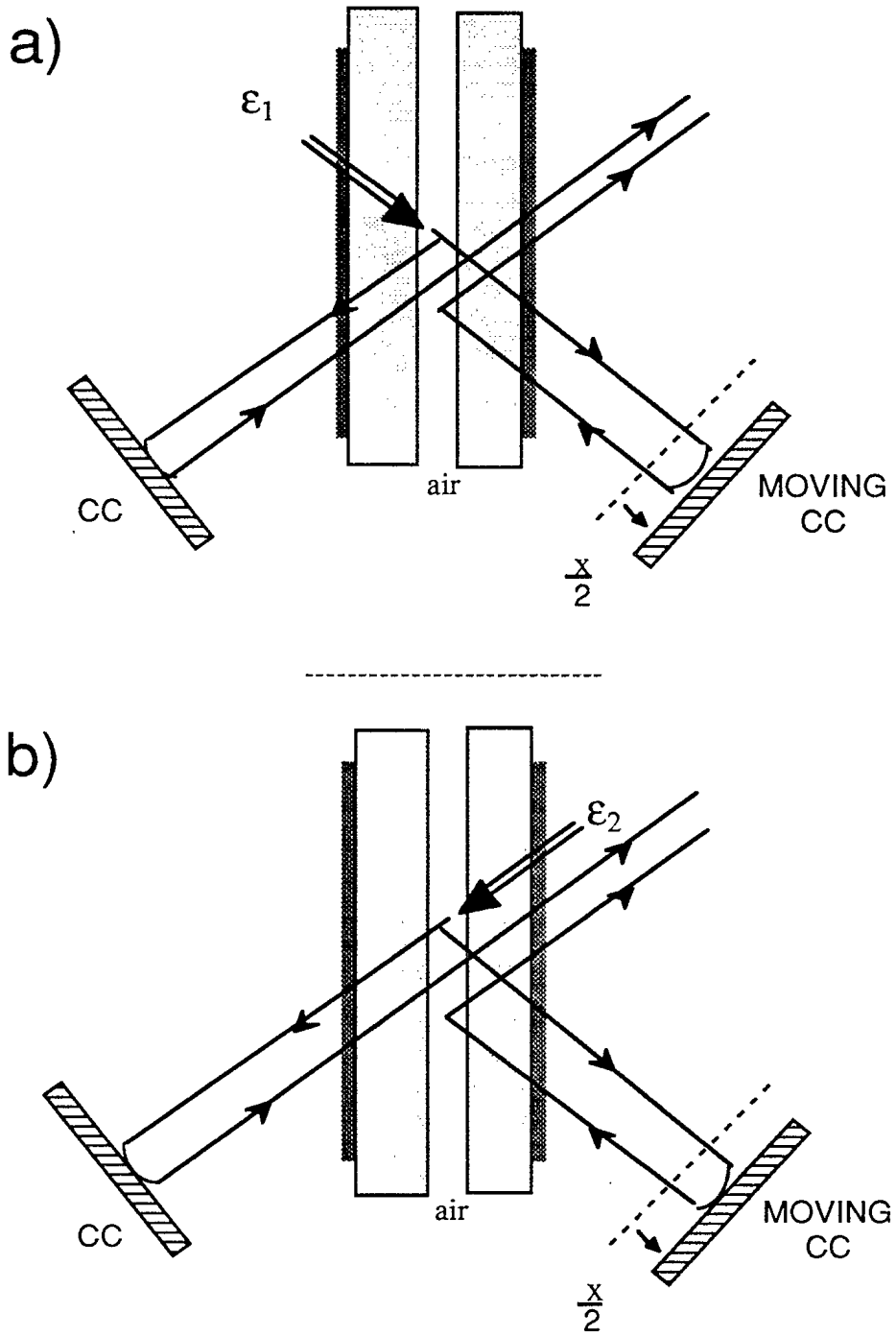

FIGURE 10- Ray tracings representing the two internal emission components ε_1 and ε_2 (see text) from substrate-1 (a) substrate-2 (b), respectively

$$\text{RAW SPEC}(\varepsilon_2) = \mathbf{K}_2 \frac{(1 - T_{c2}\, T_{s2})}{T_{c2}\, T_{s2}} B_s \qquad [67b]$$

where the complex responsivity $\mathbf{K}_2$ defined by eq. 60 has been introduced. Inspection of eqs. 65a and 67a shows that the two modulation terms are 180 degree out of phase and cancels out when the two substrates and their corresponding AR coatings are optically identical, i.e. if

$$T_{c1} = T_{c2} \qquad [68]$$

$$T_{s1} = T_{s2} \qquad [69]$$

then

$$\text{MODULATION}(\varepsilon_1) = - \text{MODULATION}(\varepsilon_2), \qquad [70]$$

which means that the real substrate emissions are not detected at the interferogram level when the two substrates (and AR coatings) are optically identical.

4.5 Self-Emission from the Splitting Layer

The last important source of self-emission arises from the splitting layer itself where graybody radiation and stray light can emanate from the layer and interfere with itself. In the proposed beamsplitter configuration (Section 4.3) the splitting layer is constituted by a thin film of air which is totally transparent. Consequently, there is no self-emission expected from this air layer. However, for the sake of completeness we present a simple analytical method for evaluating this self-emission contribution when the splitting layer is absorbing. To our knowledge, such a method has not been reported in the past. Our approach can be used to compute the self-emissions of a wide range of splitting layer configurations.

We will assume that the splitting layer is absorbing with a complex refractive index $\mathbf{n}_1 = n_1 - ik_1$, a thickness d, and is symmetrically bounded by identical transparent media of index n_0. Figures 11a and 11b represent the layer together with parameters used to model the phenomenon. The bulk material composing the layer generates (emission and stray light) isotropic IR radiation. Only the radiation inside the field of view of the detector will

contribute to the interferogram. The only two components that can contribute to the interferogram are indicated in Figs. 11a and 11b where ε_{in} is defined as the emitted intensity (radiance units) of the bulk material. For each direction, this emitted intensity generates two beams of amplitudes $\mathbf{e}_1$ and $\mathbf{e}_2$ as a result of the multiple reflections inside the layer. After reflections on the two corner reflectors such as for usual interferometer ray tracings (see Figs. 8a and 8b), the two beams are recombined for interference at the detector level.

For the emitted intensity contribution in direction of the fixed corner reflector (Fig. 11a) the amplitude $\mathbf{e}_1$ of the first beam can be evaluated by adding the multiple reflections intervening inside the layer. Following Heavens (Ref. 8) and according to the Fresnel coefficients, defined in Fig. 11, this amplitude is given by

$$\mathbf{e}_1 = \sqrt{\varepsilon_{in}}\left(t'_1 + r'^2_1\, t'_1\, e^{-2\alpha}\, e^{-2i\Delta} + r'^4_1\, t'_1\, e^{-4\alpha}\, e^{-4i\Delta} + \ldots\right) \qquad [71]$$

where

$$\Delta = 2\,\pi\,\nu\, n_1^{eff}\, d\, \cos(\theta_1) \qquad [72]$$

and

$$\alpha = 2\,\pi\,\nu\, k_1^{eff}\, d\, \cos(\theta_1). \qquad [73]$$

The effective refractive index (n^{eff}_1) and effective absorption coefficient (k^{eff}_1) can be derived from the Snell law. Knowing that $r'_1 = -r_1$, and adding terms in eq. 71 yields

$$\mathbf{e}_1 = \sqrt{\varepsilon_{in}}\,\frac{t'_1\, e^{-\alpha}\, e^{-i\Delta}}{\left(1 - r_1^2\, e^{-2\alpha}\, e^{-2i\Delta}\right)} \qquad [74]$$

which can be expressed in a more compact form using the amplitude transmittance ($\mathbf{t}$) expression of the layer defined by eqs. 38 and 41, i.e.

$$\mathbf{e}_1 = \sqrt{\varepsilon_{in}}\,\frac{\mathbf{t}}{t_1}\, e^{\alpha}\, e^{i\Delta}\ . \qquad [75]$$

From similar considerations, the amplitude $\mathbf{e}_2$ of the second beam (Fig. 11a) is found to be

$$\mathbf{e}_2 = \sqrt{\varepsilon_{in}}\left(\, r'^2_1\, e^{-\alpha}\, e^{-i\Delta}\, t'_1 \; + r'^3_1\, t'_1\, e^{-3\alpha}\, e^{-3i\Delta} + \ldots\right) \qquad [76]$$

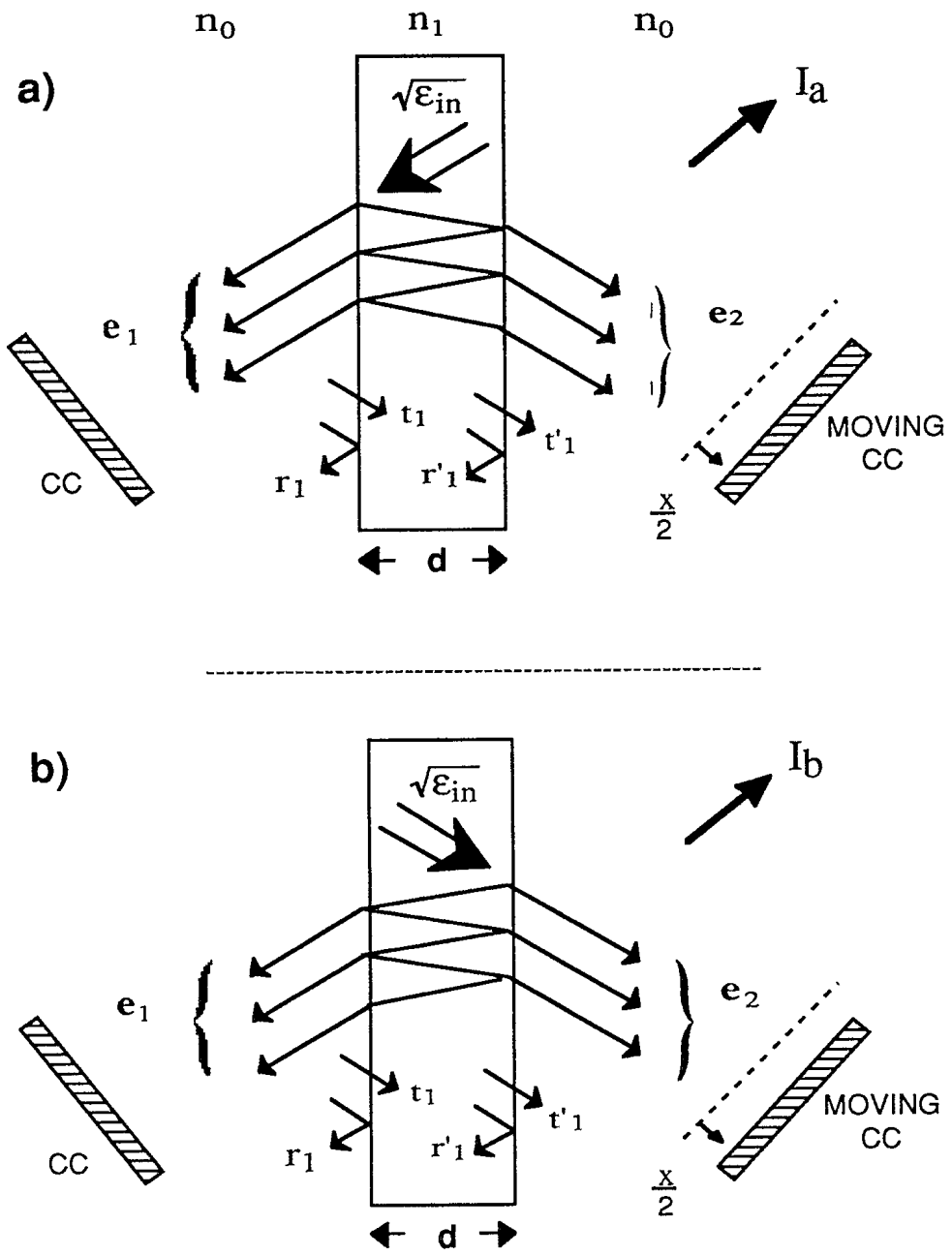

FIGURE 11- Ray tracings for the modelization of the self-emission from the splitting layer. Graybody radiation and stray light can emanate from the layer and interfere with itself to create a significant contribution to the raw spectrum (see text).

resulting in after addition

$$\mathbf{e}_2 = \sqrt{\varepsilon_{in}}\,\frac{-\,r_1\,t'_1\,e^{-\alpha}\,e^{-i\Delta}}{\left(1 - r_1^2\,e^{-2\alpha}\,e^{-2i\Delta}\right)} \qquad [77]$$

which can be expressed in a compact form using the layer transmittance (**t**) defined by eqs. 38 and 41,

$$\mathbf{e}_2 = \sqrt{\varepsilon_{in}}\left(\frac{-r_1}{t_1}\right)\mathbf{t}\ . \qquad [78]$$

Consequently, the output amplitudes corresponding to the two interfering beams associated with this self-emission component (Fig. 11 a) are

$$\mathbf{A}_1 = \mathbf{e}_1\,\mathbf{t} = \sqrt{\varepsilon_{in}}\,\frac{\mathbf{t}^2}{t_1}\,e^{\alpha}\,e^{i\Delta} \qquad [79]$$

$$\mathbf{A}_2 = \mathbf{e}_2\,\mathbf{r}\,e^{\,i\phi} = \sqrt{\varepsilon_{in}}\left(\frac{-r_1}{t_1}\right)\mathbf{t}\,\mathbf{r}\,e^{\,i\phi} \qquad [80]$$

which yields

$$\mathbf{A}_1 + \mathbf{A}_2 = \sqrt{\varepsilon_{in}}\,\frac{\mathbf{t}}{t_1}\left(\mathbf{t}\,e^{\alpha}\,e^{i\Delta} - r_1\,\mathbf{r}\,e^{\,i\phi}\right) \qquad [81]$$

The associated intensity I_a is found by multiplying eq. 81 by its complex conjugate leading to

$$I_a = \varepsilon_{in}\,\frac{T}{T_1}\left[\,T\,e^{2\alpha} + RR_1 - r_1\,e^{\alpha}\left(\mathbf{r}\,\mathbf{t}^*\,e^{\,i(\phi-\Delta)} + \mathbf{r}^*\,\mathbf{t}\,e^{-i(\phi-\Delta)}\right)\right] \qquad [82]$$

where capital letters representing intensities are defined as $T = \mathbf{t}\,\mathbf{t}^*$, $R = \mathbf{r}\,\mathbf{r}^*$ and $R_1 = r_1\,r_1$.

For the case in which the emitted intensity contribution is in the direction of the moving corner reflector (Fig. 11b), the two amplitudes $\mathbf{e}_1$ and $\mathbf{e}_2$ are simply the reverse situation of Fig. 11a. In this case, we have

$$\mathbf{e}_1 = \sqrt{\varepsilon_{in}}\left(\frac{-r_1}{t_1}\right)\mathbf{t} \qquad [83]$$

$$\mathbf{e}_2 = \sqrt{\varepsilon_{in}}\,\frac{\mathbf{t}}{t_1}\,e^{\alpha}\,e^{i\Delta} \qquad [84]$$

which yields for the two output amplitudes interfering at the detector level

$$\mathbf{A}_1 = \mathbf{e}_1\,\mathbf{t} = \sqrt{\varepsilon_{in}}\,\left(\frac{-r_1}{t_1}\right)\mathbf{t}^2 \qquad [85]$$

$$\mathbf{A}_2 = \mathbf{e}_2\,\mathbf{r}\,e^{i\phi} = \sqrt{\varepsilon_{in}}\,\frac{\mathbf{r}\,\mathbf{t}}{t_1}\,e^{\alpha}\,e^{i\Delta}\,e^{i\phi}\,. \qquad [86]$$

Adding these two output amplitudes and multiplying the result by its complex conjugate gives the corresponding output intensity I_b (Fig. 11b) incident on the detector

$$\mathbf{A}_1 + \mathbf{A}_2 = \sqrt{\varepsilon_{in}}\,\frac{\mathbf{t}}{t_1}\left(-r_1\,\mathbf{t} + \mathbf{r}\,e^{\alpha}\,e^{i(\phi+\Delta)}\right) \qquad [87]$$

and

$$I_b = \varepsilon_{in}\,\frac{T}{T_1}\left[\,R\,e^{2\alpha} + TR_1 - r_1\,e^{\alpha}\left(\mathbf{r}\,\mathbf{t}^*\,e^{i(\phi+\Delta)} + \mathbf{r}^*\,\mathbf{t}\,e^{-i(\phi+\Delta)}\right)\right]\,. \qquad [88]$$

The quantities of interest in eqs. 82 and 88 are the two modulated components which add together to produce the interferogram corresponding to the layer self-emission. Defining this self-emission as $\mathbf{E}_{lay}$ it follows that

$$\mathbf{E}_{lay} = \varepsilon_{in}\,\frac{T}{T_1}\,(-r_1\,e^{\alpha})\left[\,\mathbf{r}\,\mathbf{t}^*\,e^{i\phi}\left(e^{-i\Delta} + e^{i\Delta}\right) + \mathbf{r}^*\,\mathbf{t}\,e^{-i\phi}\left(e^{-i\Delta} + e^{i\Delta}\right)\right] \qquad [89]$$

or

$$\mathbf{E}_{lay} = \varepsilon_{in}\,\frac{T}{T_1}\left(-r_1\,e^{\alpha}\,2\cos\Delta\right)\left[\,\mathbf{r}\,\mathbf{t}^*\,e^{i\phi} + \mathbf{r}^*\,\mathbf{t}\,e^{-i\phi}\,\right]\,. \qquad [90]$$

To further reduce eq. 90 it is convenient to use again the connecting relation between **t** and **r** (eq. 42) but for and absorbing layer i.e.

$$\mathbf{t} = \mathbf{r}\,\mathbf{H}\,e^{i\pi/2} \qquad [91]$$

where now **H** is a complex number given by

$$\mathbf{H} \equiv H\, e^{i\,\theta_H} = \left(\frac{1 - r_1^2}{r_1}\right) \frac{1}{\left(e^{\alpha}\, e^{-i\Delta} - e^{-\alpha}\, e^{i\Delta}\right)} \quad . \qquad [92]$$

Note that eq. 92 is directly obtained by inserting the complex phase associated with an absorbing layer, $\delta = \Delta - i\alpha$, into eq. 43 and where Δ an α are defined by eqs. 72 and 73, respectively. Taking eq. 92 into account and using eq. 91 into eq. 90 yields

$$\mathbf{E}_{lay} = \varepsilon_{in} \frac{T}{T_1} \left(-r_1\, e^{\alpha}\, 2 \cos \Delta\right) \left[\, \mathbf{r}\, \mathbf{r}^*\, H\, e^{\,i\left(\phi - \frac{\pi}{2} - \theta_H\right)} + \mathbf{r}^*\, \mathbf{r}\, H\, e^{\,-i\left(\phi - \frac{\pi}{2} - \theta_H\right)} \right] \qquad [93]$$

or in a simpler form

$$\mathbf{E}_{lay} = \varepsilon_{in} \frac{T}{T_1} \left(\, r_1\, e^{\alpha}\, 2 \cos \Delta\right) (2\, R\, H) \cos\left(\, \phi + \frac{\pi}{2} - \theta_H \right) \qquad [94]$$

where again $R = \mathbf{r}\, \mathbf{r}^*$ and H together with θ_H are defined by eq. 92.

As defined, eq. 94 gives an analytical expression for the self-emission of the layer composing the beamsplitter. It should be emphasized that eq. 94 is not rigorously exact mainly due to the fact the phase shift associated to the air-layer reflection, r_1, was neglected in the development. This phase shift becomes important for strongly absorbing layer. Thus eq. 94 constitutes a good approximation for slightly absorbing layer materiel which is usually the case because this is the condition that maximizes the sensitivity of the interferometer. In addition, for slightly absorbing layer material θ_H becomes negligible. Consequently, the self-emission interferogram (eq. 94) appears to have an extra phase of 90 degrees over the source interferogram.

Finally, the driving term in eq. 94 is the emitted intensity ε_{in} defined as the graybody radiation and stray light emanating from the bulk of the material composing the layer. For a well-designed beamsplitter the scattering inside the splitting layer is usually negligible eliminating the stray light contribution. Consequently, the only significant contribution to the emitted intensity ε_{in} arises from the graybody emission of the layer material, which is defined as

$$\varepsilon_{in} = \left(1 - e^{-2\alpha}\right) B(T_{BS}) \qquad [95]$$

where $B(T_{BS})$ is the Planck radiance corresponding to the temperature of the beamsplitter T_{BS} and 2α is the optical depth (see eq. 73) associated with the layer material. In the proposed beamsplitter configuration (Section 4.3), the splitting layer is constituted by a film of air which is totally transparent. Consequently, for the proposed beamsplitter there is no self-emission associated to the layer itself because

$$\alpha = 0, \qquad [96]$$

$$\varepsilon_{in} = 0, \qquad [97]$$

and consequently,

$$\mathbf{E}_{lay} = 0\,. \qquad [98]$$

In conclusion, for the proposed beamsplitter design the self-emission from the splitting layer vanishes.

5.0 EXPERIMENTAL PROTOTYPE: RESULT AND DISCUSSIONS

In order to evaluate the performance of an optimized FTIR spectrometer i.e. for self-emission suppression and simplified radiometric calibration, we have specified an instrument referred to as the Compact ATmospheric Sounding Interferometer, which was built under a contract with BOMEM. The primary but not exclusive application of this instrument is for the passive remote sensing of target vapors (see Ref. 5). In the following section, a description of the CATSI prototype and a discussion on its measured characteristics are presented as a validation of the proposed FTIR configuration described in this document.

5.1 Description of the CATSI prototype

The specifications of the instrument were made to agree with the three conditions of optimization defined by eqs. 26 to 28. For that, the optical configuration of the two input ports (mirrors and windows) was made as symmetric as possible to ensure the same beam attenuations and the same self-emissions in both ports. The selected beamsplitter

configuration was the one presented in Section 4.3 made of an optically thin layer of air squeezed between two thick substrates properly covered with antireflection coatings on their external faces.

More precisely, the CATSI prototype is made of two identical 4-in. diameter Newtonian telescopes optically coupled to the dual-beam interferometer. Figure 12 summarizes the optical design and shows the instrument mounted on a tripod. An important effort was done to respect symmetry criteria. The CATSI system allows measurements of spectra according to the following specifications: scene fields of view from 4 to 11 mrad, spectral coverage from 3 to 18 μm, and a spectral resolution of 1 cm^{-1} or greater. A flat plate mirror placed in front of each telescope can be rotated to the selected scene. The pointing capability of this scene mirror allows azimuth measurements from 0 to 180 degrees. Coarse adjustments in azimuth and elevation are simply achieved by rotating the whole assembly mounted on a tripod. After reflection on the scene mirror the input beam is focused by the Newtonian telescope at the entrance of the interferometer and then reflected by an off-axis parabolic mirror to produce a collimated beam of proper diameter in front of the beamsplitter. A double pendulum scanning mechanism controls the periodic displacement of the two corner reflectors (CC) that generates the interferogram. The beamsplitter consists of a thin air gap ($\lambda/4$ at 7 μm) squeezed between two ZnSe substrates having antireflection coatings on their external faces. Of the two output channels only one is used at this moment. This output module contains parabolic and condensing mirrors that focus the beam onto a sandwich MCT-InSb detector (1 mm) mounted on a microcooler (EG&G Judson): The MCT element is optimized for the 6-18 μm spectral region, while the InSb element is optimized for the 2-5 μm region. Two CCD cameras mounted on the top of the two telescope modules can be used to aim and view the scenes under consideration. With this instrument, two scenes coming from adjacent FOVs are optically combined at the detector level yielding the spectral residual of the scenes. The overall system forms a cube of approximately 30 cm^3 and weights 18 kg.

5.2. Results: Instrument responsivities and residual

In Chapter 3 we have defined two basic requirements to obtain an optimized FTIR spectrometer. The first requirement implies that the self-emissions produced by the optical components of the two input ports (excluding beamsplitter components) must be symmetrically the same. After a careful experimental investigation with the CATSI prototype we came to the conclusion that there is no major difficulty to achieve the desired symmetry

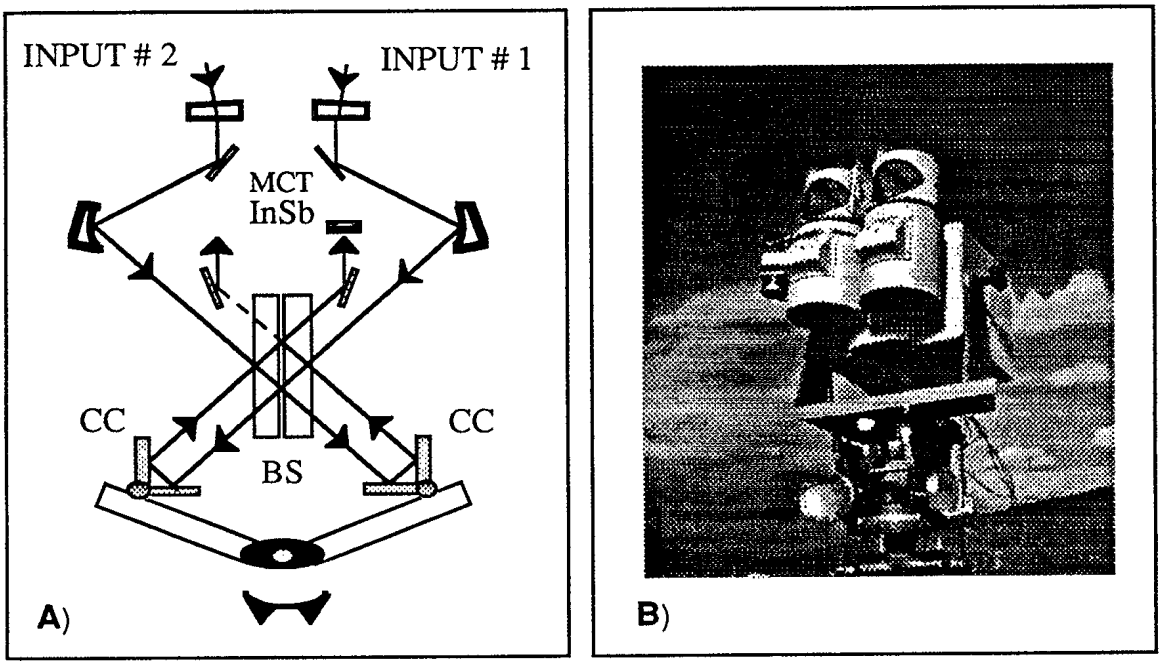

FIGURE 12- Optical diagram and a picture of the Compact Atmospheric Sounding Interferometer (CATSI)

between the two input optics, i.e. the two related self-emissions are quite balanced. Rather, the main limitation appeared to come essentially from the beamsplitter itself. The remaining part of this document emphasizes this point by showing the impact of the beamsplitter accuracy on the performance of the CATSI prototype.

In Chapter 3.0 it has been established that the raw spectrum S delivered by a double-beam interferometer of this type can be defined referring to input-1 characteristics,

$$S = K_1 (L_1 + O_1), \qquad [99]$$

$$O_1 = \left(SE_{in1} + \frac{K_2}{K_1} L_2 + \frac{K_2}{K_1} SE_{in2} + \frac{E_{BS}}{K_1} \right) \qquad [100]$$

or alternately with the characteristics of input-2

$$S = K_2 (L_2 + O_2), \qquad [101]$$

$$O_2 = \left(SE_{in2} + \frac{K_1}{K_2} L_1 + \frac{K_1}{K_2} SE_{in1} + \frac{E_{BS}}{K_2} \right) \qquad [102]$$

where we remember that L_1 and L_2 are the two target source radiances with K_1, K_2 and SE_{in1}, SE_{in2} defined as the responsivities and the self-emissions associated with input-1 and input-2, respectively. For this particular configuration of beamsplitter that uses a thin layer of air as a splitting layer it has been shown (Section 4.5) that in this case the self-emission term $E_{lay} = 0$ yielding $E_{BS} = 0$ and consequently,

$$O_1 = \left(SE_{in1} + \frac{K_2}{K_1} L_2 + \frac{K_2}{K_1} SE_{in2} \right), \qquad [103]$$

$$O_2 = \left(SE_{in2} + \frac{K_1}{K_2} L_1 + \frac{K_1}{K_2} SE_{in1} \right). \qquad [104]$$

Note that the two substrate self-emission contributions are included in the input port emission, SE_{in1} and SE_{in2}.

The experimental measurement of K_1, K_2 and O_1, O_2 provides a quantitative approach to evaluate the compensation characteristics of the interferometer. For that the two-temperature calibration method described in Chapter 3.0 was applied. Figures 13a represents the modules of the measured responsivities for input-1 and input-2. The good agreement between the two spectra from 700 to 3000 cm^{-1} confirms the high level of symmetry obtained with the proposed FTIR spectrometer configuration. Fig. 13b compared the modules of two measured offsets obtained when the calibration is done on input-1 (O_1) or alternatively when it is done on input-2 (O_2) for the case in which both inputs look exactly at the same source of radiance $L = L_1 = L_2$ (blackbody at 15° C). From inspection of eqs. 103 and 104 it is concluded that this good agreement between the two offsets and L in the spectral region from 700 to 3000 cm^{-1} is consistent with these conditions $K_1 = - K_2$ and $SE_{in1} = SE_{in2}$ yielding $O_1 = - L$ and $O_2 = - L$, as observed in Fig. 13b.

Another way to look at the optical subtraction capability of the instrument is provided by a suitable recast of eq. 101 (taking input-2 as a reference) in a more convenient format, i.e.

$$S = K_2 (\delta L + re_2), \qquad [105]$$

where $\delta L = L_2 - L_1$, and re_2 accounts for a possible optical asymmetry and is defined as the instrument residual given by

$$re_2 = \left(1 + \frac{K_1}{K_2}\right) L_1 + \left(SE_{in2} + \frac{K_1}{K_2} SE_{in1}\right). \qquad [106]$$

In this case, the calibration equation for a dual beam interferometer operating in differential detection mode is given by

$$\delta L = \left(\frac{S}{K_2} - re_2\right). \qquad [107]$$

Figure 13c shows an example of the measured instrument residual re_2 (bottom curve). For an ideal instrument this residual should be zero throughout the spectrum. For our prototype it has been found that the instrument residual (unbalance) is not exactly zero but usually smaller than 2 % in the region from 700 to 3000 cm^{-1} (3.5 - 15 μm). This is approximately a factor of 10 smaller than the instrument residual measured on a conventional double-beam interferometer (BOMEM MB-100) in certain spectral region. However, there is an unexpected strong residual in the from 500 to 700 cm^{-1} (see Fig. 13c). After an extensive investigation we came to the conclusion that these imperfections (2 % and strong residual) come from the limited performance of the manufactured beamsplitter (prototype). An undesired dissymmetry between the optical properties of the two ZnSe substrates forming the beamsplitter was found. This is partly due to non-identical antireflection coatings present on the external faces of each substrate, and partly due to a difference between the transmission associated with each substrate. Both effects introduce a dissymmetry in the self-emission and the attenuation associated with each input. A useful model which predicts the instrument residual re_2 in terms of the substrate characteristics is presented and validated in Section 5.3. In this model the instrument residual is directly given by

$$re_2 = \left(1 + \frac{K_1}{K_2}\right)[\, L_1 - B_s \,]. \qquad [108]$$

This relation entirely defines the instrument residual in terms of the beam splitter temperature (B_S), the source radiance (L_1) and the responsivity ratio. Although the ultimate performance of the CATSI prototype has not been reached yet due to manufacturing imperfections in the actual beamsplitter, the previous relations indicate that these imperfections can be predicted and compensated for in real time, provided that the beamsplitter temperature is known and that the responsivities ratio is well characterized. Fortunately, the CATSI system already contains a temperature sensor installed on the beamsplitter mount. The responsivity ratio can be accurately evaluated by application of the two-temperature calibration method. Moreover, if the temperature dependence of the beamsplitter spectral responsivity is predefined (from proper measurements) then the full calibration of CATSI spectra can be performed in real time without any additional measurements which reduces by a factor of 3 the number of operations necessary to generate a calibrated spectrum.

Finally, from the previous discussion and by extension of eq. 32, it follows that the calibrated spectrum generated in real time with the CATSI prototype, for the single-beam operation mode, is given by

$$L_2 = \frac{S}{K_2(T_{BS})} + L_1 - re_2(T_{BS}) \qquad [109]$$

or for the differential operation mode

$$\delta L = \frac{S}{K_2(T_{BS})} - re_2(T_{BS}) \qquad [110]$$

where it is convenient to recall that S is the measured raw spectrum (complex), $K_2(T_{BS})$ is the complex responsivity and $re_2(T_{BS})$ is the instrument residual, both calibration parameters being determined by the beamsplitter temperature. Although the CATSI prototype was conceived to be fully consistent with the proposed Fourier spectrometer configuration, it was not possible to reach the ultimate performance ($re_2 = 0$) due to the optical asymmetry between the two beamsplitter substrates discussed above. This technical imperfection in the beamsplitter manufacturing can be easily eliminated by a better control of the optical characteristics of the paired substrates. Unfortunately, there was no other CATSI beamsplitter (of this type) available to verify this asymmetry hypothesis. However, in the next

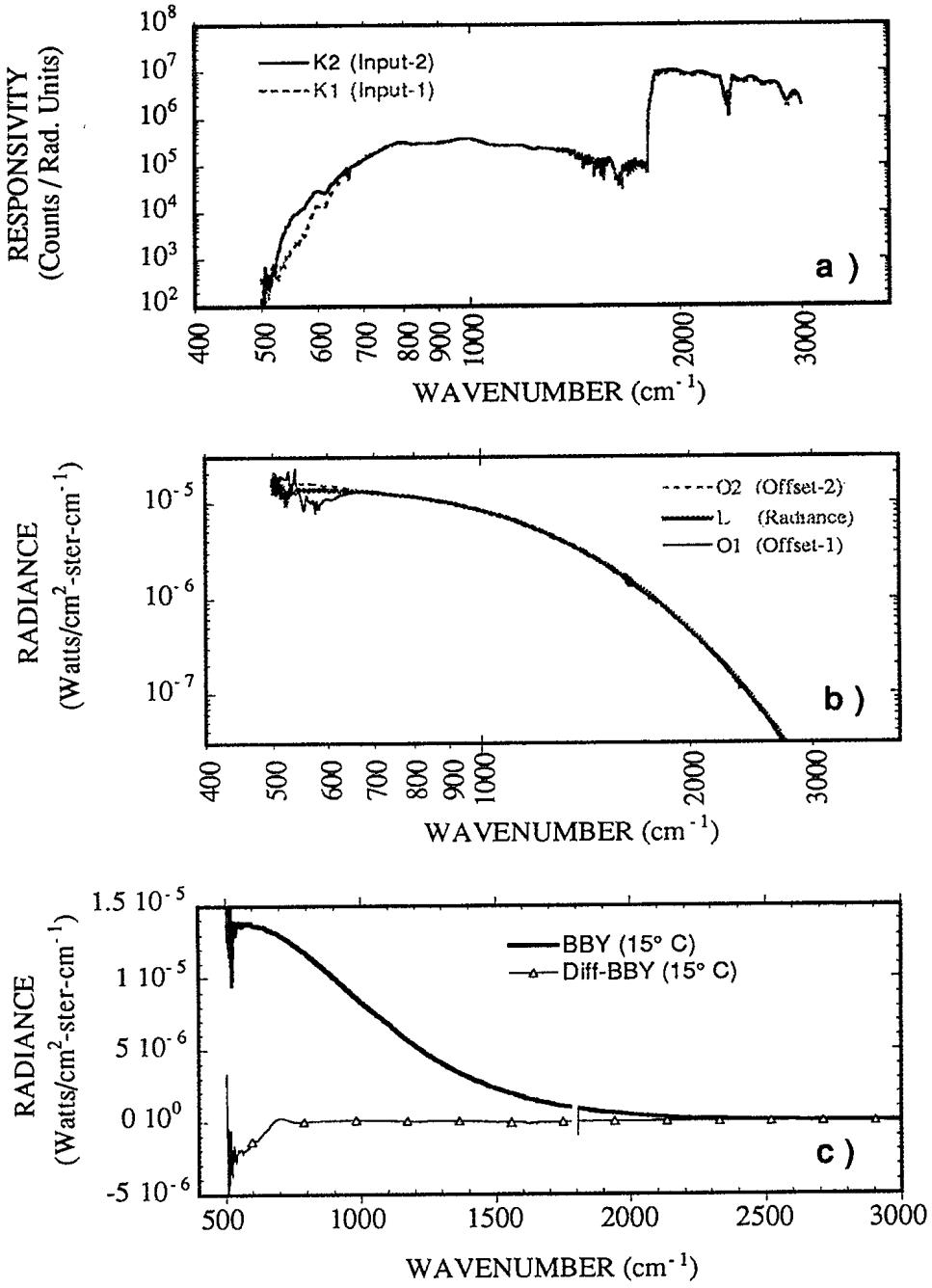

FIGURE 13 - Spectral responsivities (a) and offsets (b) associated with each of the two optical channels of CATSI system. Fig. 13c compares the single port measurement of a blackbody at 15°C (upper curve) and the resulting difference when the two ports are utilized.

Section, we show that the modeling of the instrument residual based on the beamsplitter asymmetry agrees very well with the observed data.

5.3 Modeling of the Instrument Residual

To evaluate the instrument residual $\mathbf{re}_2$ from the substrates dissymmetry discussed in Section 5.2 (eq. 108), we first use the results established at eqs. 65b and 67b where it was found that the raw spectrum associated to the self-emission of each substrate was given by

$$\mathbf{K}_1 \frac{(1 - T_{c1}T_{s1})}{T_{c1}T_{s1}} B_s \qquad [111]$$

and

$$\mathbf{K}_2 \frac{(1 - T_{c2}T_{s2})}{T_{c2}T_{s2}} B_s \qquad [112]$$

for substrate-1 (fixed corner reflector side) and substrate-2 (moving corner reflector side), respectively. It is remembered that T_{c1}, T_{c2} and T_{s1} , T_{s2} represent the transmittances of the associated AR coatings and substrates. B_s is the plank radiance related to the substrate temperature. In this case, if input-1 and input-2 look at target sources of radiance L_1 and L_2, respectively, the resulting raw spectrum is given by

$$\mathbf{S} = \mathbf{E}_1 + \mathbf{E}_2 \qquad [113]$$

with

$$\mathbf{E}_1 = \mathbf{K}_1 \left[L_1 + \frac{(1 - T_{c1}T_{s1})}{T_{c1}T_{s1}} B_s \right], \qquad [114]$$

$$\mathbf{E}_2 = \mathbf{K}_2 \left[L_2 + \frac{(1 - T_{c2}T_{s2})}{T_{c2}T_{s2}} B_s \right]. \qquad [115]$$

To obtain these two equations it is assumed that the main source of uncompensated (or unsuppressed) self-emission comes from the beamsplitter substrates alone, i.e. other self-emissions from the two input components cancels out. Rewriting eq. 113 to obtain the raw spectrum in terms of the instrument residual $\mathbf{re}_2$ (see eq. 105) yields

$$S = K_2 (\delta L + re_2), \qquad [116]$$

or

$$S = K_2 \left[\delta L + \left(1 + \frac{K_1}{K_2}\right) L_1 + \frac{K_1}{K_2} \frac{(1 - T_{c1}T_{s1})}{T_{c1}T_{s1}} B_s + \frac{(1 - T_{c2}T_{s2})}{T_{c2}T_{s2}} B_s \right]. \qquad [117]$$

Further simplifications occur by using the results established in eqs. 59 and 60 where it was found that the ratio of the two responsivities is given by

$$\frac{K_1}{K_2} = - \frac{T_{c1}T_{s1}}{T_{c2}T_{s2}} \qquad [118]$$

which after insertion into eq. 117 yields

$$re_2 = \left(1 - \frac{T_{c1}T_{s1}}{T_{c2}T_{s2}}\right) [L_1 - B_s] \qquad [119]$$

or alternately

$$re_2 = \left(1 + \frac{K_1}{K_2}\right) [L_1 - B_s]. \qquad [120]$$

As a validation of this modeling, Figs. 14 and 15 compare the measured and predicted instrument residuals (re_2) in the mid-IR and the far-IR. The measured residual is obtained from the standard two-temperature calibration method. The predicted residual (model) is calculated using eq. 120 (model). Figure 14 compares measurements and predictions (real and imaginary parts) obtained when the input source L_1 is a blackbody at a temperature of T_B=5.9° C. In Figure 15, the input source L_1 is a blackbody at a temperature of T_B=49.5° C. For both cases the beamsplitter temperature was 33° C (B_S). As predicted by eq. 120, the behavior of the residual strongly depends on the temperature difference (through L_1- B_S) between the source and the beamsplitter. For instance, in Fig. 14a a negative temperature difference of -27.1° C (i.e. 5.9° - 33°) yields a negative real part and a positive imaginary part of the residual in the region from 550 to 650 cm^{-1}. In Fig. 15a, this is the reverse situation in which a temperature difference of +16.5° C (i.e. 49.5° - 33°) yields a positive real part and a

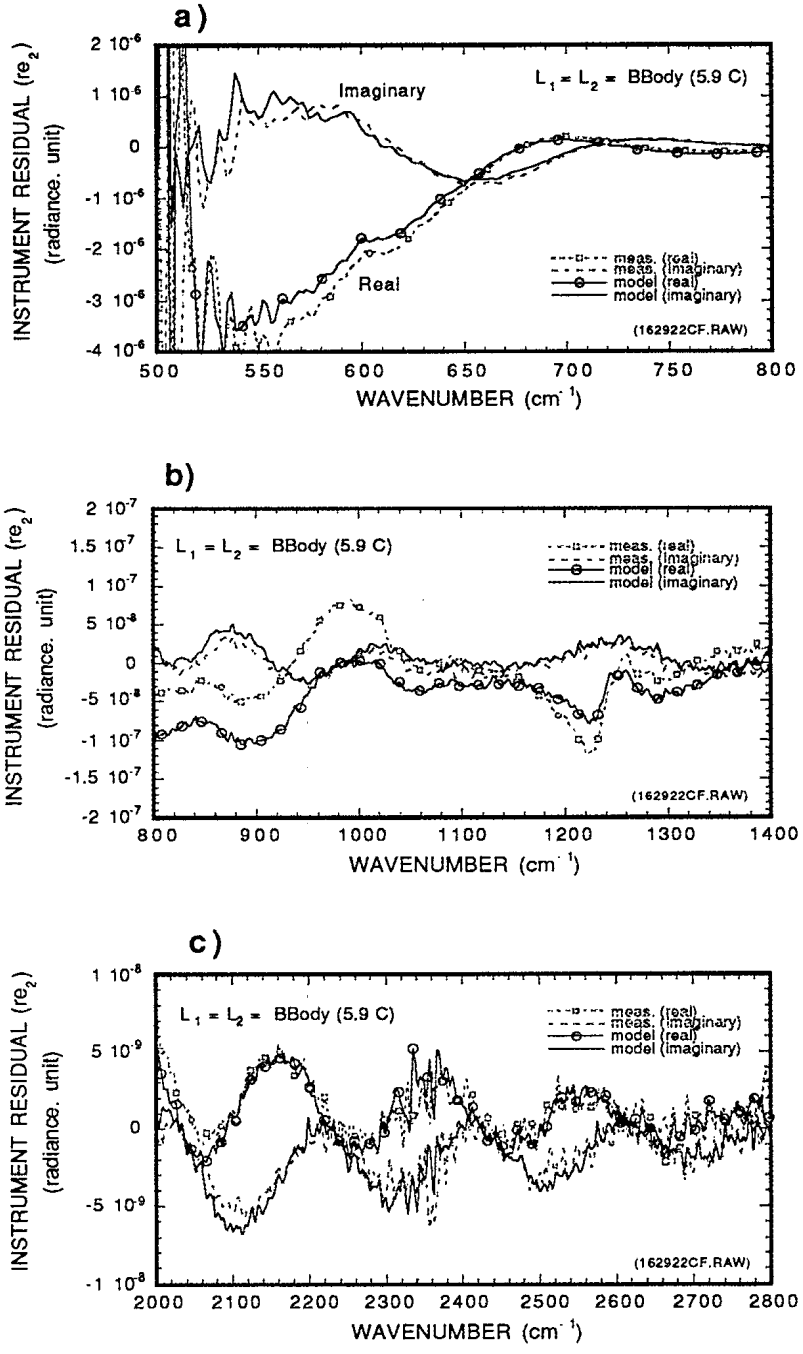

FIGURE 14 - Comparison of the measured and predicted (model: eq. 120) instrument residual obtained when the input source L_1 corresponds to a **blackbody at T_B=5.9 C** (a,b) correspond to the far IR and (c) corresponds to the mid IR

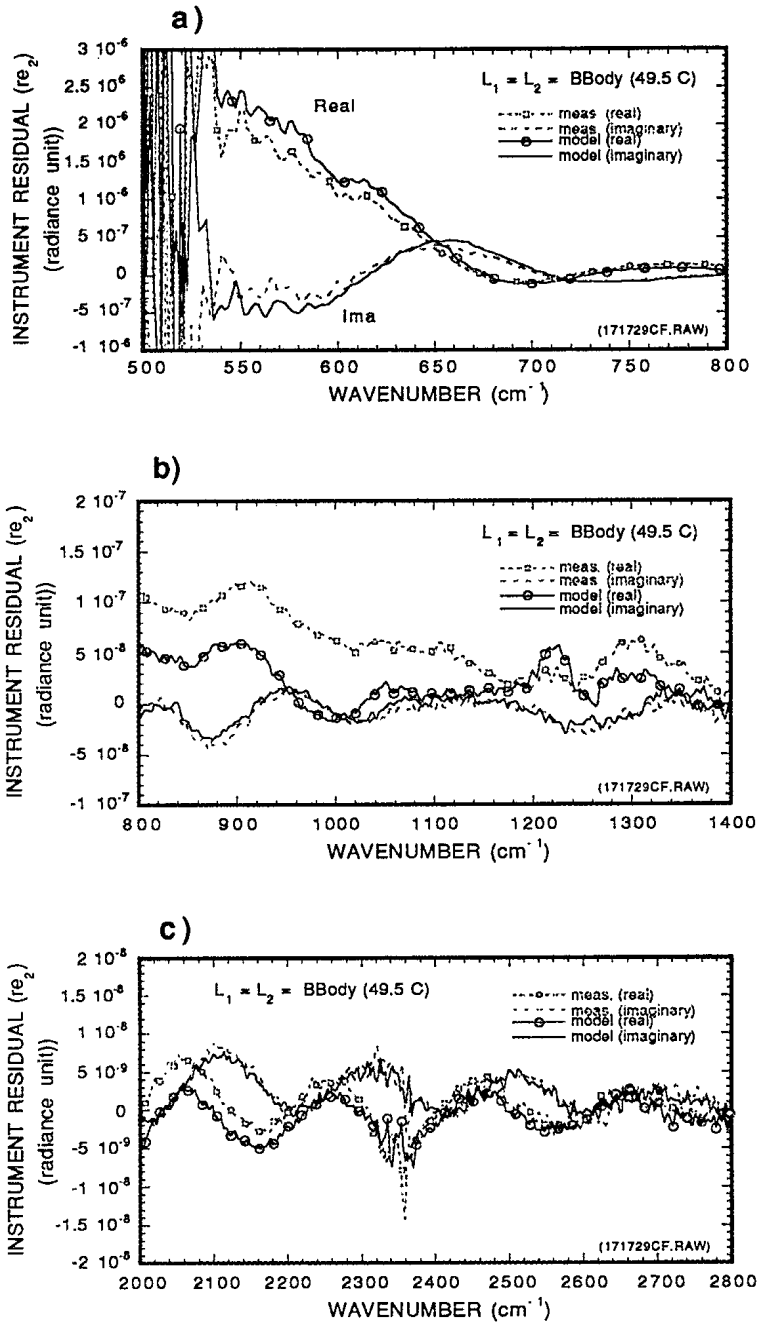

FIGURE 15 - Comparison of the measured and predicted (model: eq. 120) instrument residual obtained when the input source L_1 corresponds to a **blackbody at T_B=49.5 C** (a,b) correspond to the far IR and (c) corresponds to the mid IR

negative imaginary part of the residual. Overall the model (eq. 120) appears quite accurate to predict the behavior of the instrument residual. Many other comparisons indicate the same level of accuracy. The slight discrepancy between the models and observed in the 800-1400 cm^{-1} is believed to be due to the experimental errors present in the measurements.

5.4 Impact of Polarization on Responsivity Phases

In Section 4.3 it has been found that, for the proposed beamsplitter configuration (thin layer of air squeezed between two thick substrates), the phase difference between the two responsivities, $\mathbf{K}_1$ and $\mathbf{K}_2$, must be 180° (out of phase, see eqs. 59-60) at any wavenumber and for any dissymmetry in substrate transmissions. However, the experimental results obtained with the CATSI system do not entirely agree with this. As shown in Fig. 16, in the spectral region of strong substrate dissymmetries between 530 and 680 cm^{-1}, phase differences other than 180° appear. Figure 16 shows an example of the phases for $\mathbf{K}_1$ and $\mathbf{K}_2$ and the corresponding difference as a function of the wavenumber. In the following, this anomaly is interpreted as an effect due to the two components of polarization (s and p) interacting with the beamsplitter substrates. The equations that give the raw spectrum for a CATSI-type double-beam interferometer are

$$\mathbf{S} = \mathbf{E}_1 + \mathbf{E}_2 \qquad [121]$$

with

$$\mathbf{E}_1 = \mathbf{K}_1 (L_1 + \mathbf{S}\mathbf{E}_{in1}) \qquad [122]$$

$$\mathbf{E}_2 = \mathbf{K}_2 (L_2 + \mathbf{S}\mathbf{E}_{in2}) \qquad [123]$$

where $\mathbf{K}_1$, $\mathbf{K}_2$ and $\mathbf{SE}_{in1}$, $\mathbf{SE}_{in2}$ are defined as the responsivities and the self-emissions associated with input-1 and input-2, respectively and L_1 and L_2 are the source radiance terms. Note that the self-emission of the beamsplitter air layer is $\mathbf{E}_{BS} = 0$. Because we want to focus primarily on the effects of polarization we neglect the self-emission terms in the discussion: we pose that $\mathbf{SE}_{in1} = 0$ and $\mathbf{SE}_{in2} = 0$. In this case and according to eqs. 59-60 we have

$$\mathbf{E}_1 = K_1 e^{i\Psi} L_1 \qquad [124]$$

$$\mathbf{E}_2 = K_2 e^{i\pi} e^{i\Psi} L_2 \,. \qquad [125]$$

The two previous equations, which do not take the polarization into account, express the fact that the two complex responsivities are 180° out of phase. The equations for the case in which the two polarizations s and p are taken into account are obtained by extension of eqs. 124 and 125, yielding

$$\mathbf{E}_1 = \mathbf{E}_1^s + \mathbf{E}_1^p = \left(K_1^s\, e^{i\,\psi_s} + K_1^p\, e^{i\,\psi_p} \right) L_1 \qquad [126]$$

$$\mathbf{E}_2 = \mathbf{E}_2^s + \mathbf{E}_2^p = \left(K_2^s\, e^{i\,\psi_s} + K_2^p\, e^{i\,\psi_p} \right) e^{i\pi}\, L_2 \qquad [127]$$

Consequently, the effective responsivity modules and responsivity phases, seen by a system that measures the sum of the two components (such as CATSI), can be defined by

$$\mathbf{E}_1 \equiv K_1^{eff}\, e^{i\,\psi_1{}^{eff}}\, L_1 \qquad [128]$$

$$\mathbf{E}_2 \equiv K_2^{eff}\, e^{i\left(\psi_2{}^{eff} + \pi\right)}\, L_2 \qquad [129]$$

where

$$K_1^{eff} = \left[\left(K_1^s\right)^2 + \left(K_1^p\right)^2 + 2\, K_1^s\, K_1^p \left(\cos(\psi_s)\cos(\psi_p) + \sin(\psi_s)\sin(\psi_p) \right) \right]^{\frac{1}{2}} \qquad [130]$$

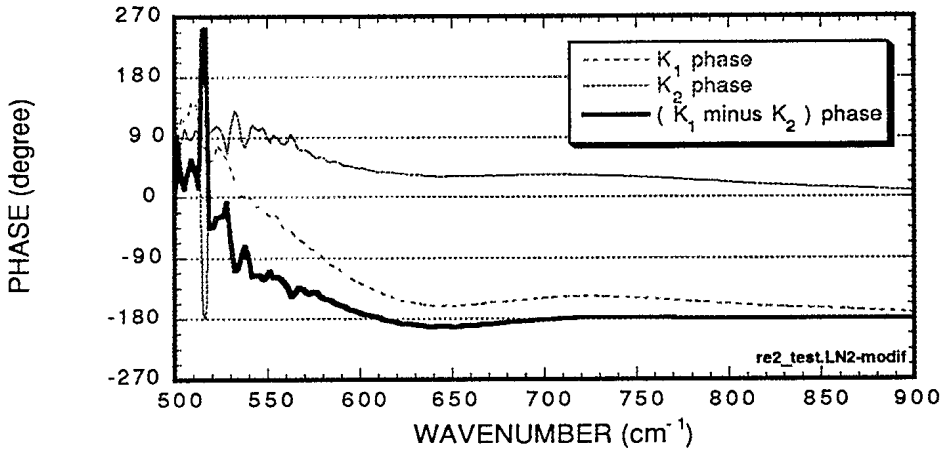

FIGURE 16 - Typical responsivity phases and the corresponding difference measured for the CATSI system

$$\tan\left(\psi_1^{eff}\right) = \frac{K_1^s \sin(\psi_s) + K_1^p \sin(\psi_p)}{K_1^s \cos(\psi_s) + K_1^p \cos(\psi_p)} \qquad [131]$$

and

$$K_2^{eff} = \left[\left(K_2^s\right)^2 + \left(K_2^p\right)^2 + 2\, K_2^s\, K_2^p \left(\cos(\psi_s)\cos(\psi_p) + \sin(\psi_s)\sin(\psi_p) \right) \right]^{\frac{1}{2}} \qquad [132]$$

$$\tan\left(\psi_2^{eff}\right) = \frac{K_2^s \sin(\psi_s) + K_2^p \sin(\psi_p)}{K_2^s \cos(\psi_s) + K_2^p \cos(\psi_p)} \; . \qquad [133]$$

From the previous equations (131 and 133) , it can be shown that the two effective responsivity phases ψ_1^{eff} and ψ_2^{eff} can differ when one of the three following conditions happen:

1- $K_1^S \neq K_2^S$ and $K_1^P = K_2^P$ and $\psi_S \neq \psi_P$,
2- $K_1^S = K_2^S$ and $K_1^P \neq K_2^P$ and $\psi_S \neq \psi_P$,
3- $K_1^S \neq K_2^S$ and $K_1^P \neq K_2^P$ and $\psi_S \neq \psi_P$.

The first two conditions arise when there is a dissymmetry in the optical transmission of the two substrates. The third condition involves the beamsplitter phase jumps (in transmission) which differ in polarization when there is absorption in the substrates and their associated AR coatings: this is a characteristic of the Fresnel coefficients for absorbing interfaces (see Heavens, Ref. 8). This yields a Responsivities Phase Difference (RPD) equal to

$$RPD = \left(\psi_2^{eff} - \psi_1^{eff} + \pi\right) \qquad [134]$$

rather than RPD = π obtained when the two substrates are non-absorbing or optically identical. In the beamsplitter of the CATSI system, the effects of polarization are observed in the 530 and 680 cm^{-1} region (Fig. 16) due the combined absorption of ZnSe substrates and thorium fluoride presents inside the AR coatings. Above 700 cm^{-1}, the beamsplitter substrates and the associated AR coatings exhibit a low level of absorption yielding a RPD = π.

5.5 Interpretation of Channel Spectrum in Instrument Residual

The aim of this section is to show that the apparent channel spectrum observed in the CATSI instrument residual $\mathbf{re}_2$ arises from a mismatch between the thickness of the two ZnSe substrates. This channel spectrum is more clearly observed in the spectral region above 1800 cm^{-1} as shown in Fig. 17. To establish the origin of this phenomenon it is convenient to use the model of spectral residual discussed in Sections. 5.2 and 5.3. In this context the instrument residual is given by (see eq. 108)

$$\mathbf{re}_2 = \left(1 + \frac{\mathbf{K}_1}{\mathbf{K}_2}\right)[\, L_1 - B_s \,]\,. \qquad [135]$$

Figure 18 exhibits the ratio of the two responsivities module $|\, \mathbf{K}_1 / \mathbf{K}_2 \,|$ corresponding to the case of Fig. 17. Equation 135 indicates that the channel spectrum observed in the instrument residual $\mathbf{re}_2$ comes from a periodic mismatch between the two responsivities. As found in eqs. 59 and 60 this responsivities ratio is directly related to the transmission of each substrate such that

$$\left|\frac{\mathbf{K}_1}{\mathbf{K}_2}\right| = \frac{T_{s1}}{T_{s2}} \qquad [136]$$

where it is assumed that the transmissions of the two AR coatings associated to each substrate are identical.

To understand the cause of this periodic mismatch between the two substrate transmissions T_{S1} and T_{S2}, we consider the interference created by the multiple reflections inside each substrate. Moreover, to simplify the problem we consider only the two main components of interference (two beam interferometry), as illustrated in Fig. 19. Taking into account this interference yields for the substrate transmissions

$$T_{s1} = T_1 \,[\, 1 + R_{ar}\, R_s \cos\,(2\pi\nu n d_1) \,] \qquad [137]$$

$$T_{s2} = T_2 \,[\, 1 + R_{ar}\, R_s \cos\,(2\pi\nu n d_2) \,] \qquad [138]$$

where d_1, d_2 and T_1, T_2 are the thickness and the single pass transmission of each substrate respectively, and n is the refractive index of the substrate material ($n \sim 2.5$ for ZnSe). R_{ar} and

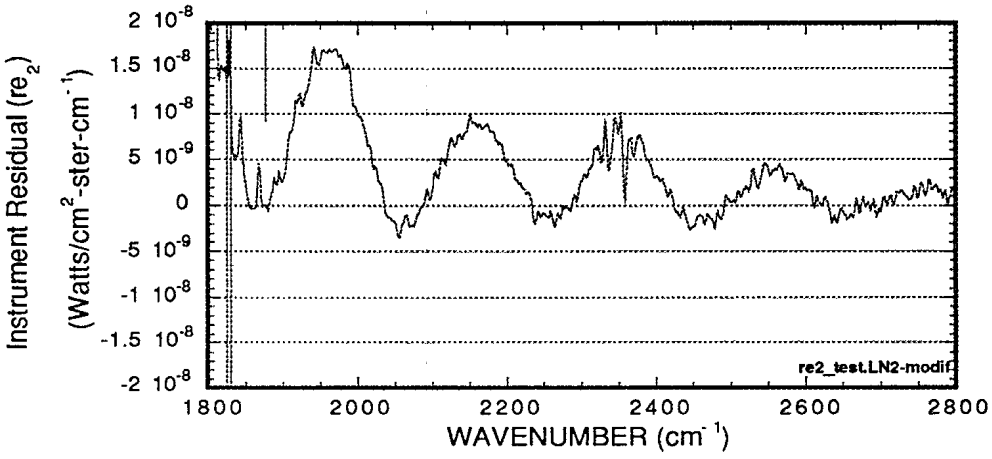

FIGURE 17 - An example of an instrument residual spectrum (real part) showing the presence of channel spectrum

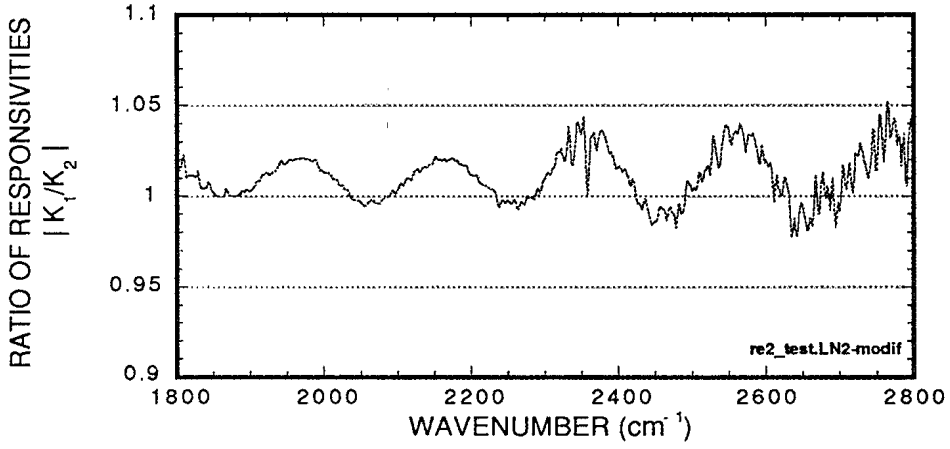

FIGURE 18 - Ratio of the two responsivities $| \mathbf{K}_1 / \mathbf{K}_2 |$ (module) showing the presence of channel spectrum

R_S are the inner reflections at the air-coating interface and the air-substrate interface, respectively. The previous equations tell that each substrate generates its own high frequency channel spectrum. Ratioing the two substrate transmissions gives

$$\frac{K_1}{K_2} = \frac{T_{s1}}{T_{s2}} = \frac{T_1 [\, 1 + R_{ar} R_s \cos (2\pi\nu n d_1) \,]}{T_2 [\, 1 + R_{ar} R_s \cos (2\pi\nu n d_2) \,]} \qquad [139]$$

which can be approximated by

$$\frac{K_1}{K_2} \approx \frac{T_1}{T_2} [\, 1 + R_{ar} R_s (\cos (2\pi\nu n d_2) - \cos (2\pi\nu n d_1)) \,] \qquad [140]$$

where only the first two terms of a Taylor expansion (denominator of eq. 139) was conserved. Simple trigonometric transformations of the previous equation leads to

$$\frac{K_1}{K_2} \approx \frac{T_1}{T_2} (1 - 2 R_{ar} R_s \sin [\pi\nu n(d_2 + d_1)] \sin [\pi\nu n(d_2 - d_1)]) \,. \qquad [141]$$

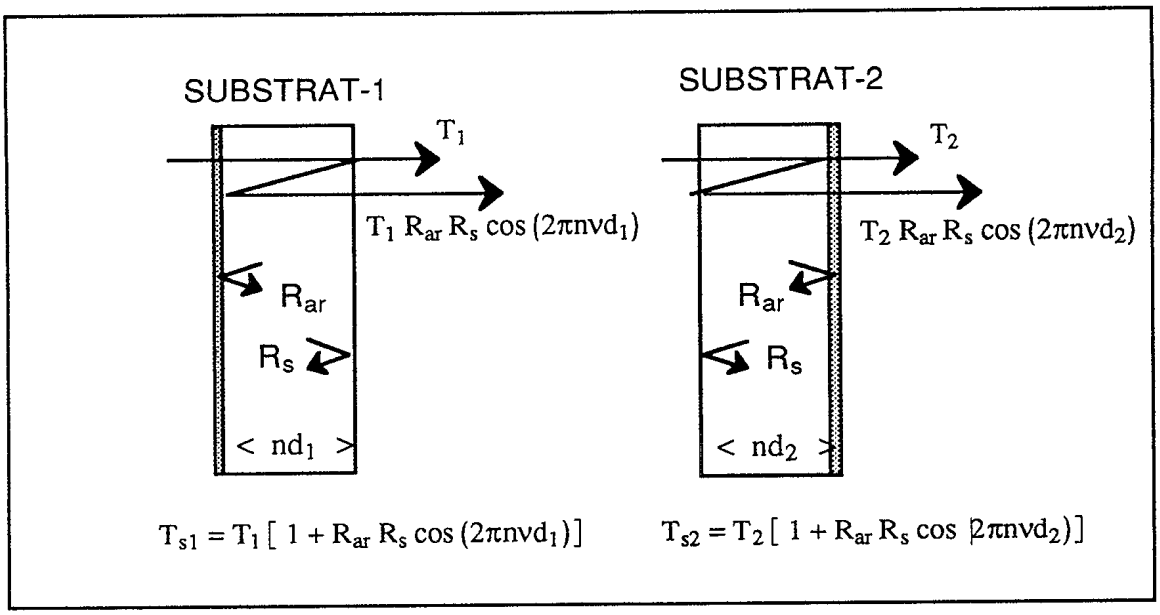

FIGURE 19 - Two beam interferometry applied to each beamsplitter substrate of CATSI and the related parameters

The first sinus term creates a high frequency modulation in the responsivities ratio spectrum. The corresponding interfringe is given by

$$\Delta \nu = \frac{1}{n\,(d_1 + d_2)} \qquad [142]$$

which leads to $\Delta \nu = 0.2\ cm^{-1}$ for the ZnSe substrates used in CATSI ($d_1 = d_2 = 1$ cm and $n = 2.5$). This high-frequency modulation can not be seen in the CATSI spectrum because the resolution of the instrument is limited to 1 cm^{-1}. The second sinus term is the cause of the channel spectrum (beating). By checkings Fig. 18 we can evaluate the interfringe to be approximately 200 cm^{-1}, yielding a thickness mismatch equals to

$$(d_2 - d_1) = \frac{1}{n\,(\Delta \nu)} = \frac{1}{2.5\,(200\ cm^{-1})} = 20\ \mu m\ . \qquad [143]$$

This result agrees quite well with the 25 μm of thickness tolerance given by the manufacturer of ZnSe substrates. The natural conclusion of this section is that there are two ways to eliminate the channel spectrum: First, by improving the thickness matching of the two substrate (ideally to better than a few microns), and second by improving the AR coating performance, i.e. making R_{ar} as small as possible, which minimizes the multiple-reflection contributions as seen in eq. 141.

6.0 EXAMPLES OF SPECTRAL MEASUREMENTS WITH CATSI

To verify the optical suppression efficiency of the CATSI instrument, a series of laboratory measurements have been performed in the differential-detection mode. For the first series, the two telescopes were aimed at the same target source, a flat plate blackbody (12"x12") approximately 3 meters away from the interferometer. Figure 20a shows examples of instrument residuals (500 to 1500 cm^{-1}) obtained for three different blackbody source temperatures 10.6° C, 33° C and 49.9° C. Also shown for comparison purposes is the measured radiance (single beam mode) corresponding to a source temperature of 10.6° C . As expected, above 750 cm^{-1} the instrument residual is quite insensitive to the source temperature and is near zero. Actually, for all three measurements the instrument residual is generally smaller than 2 % of the blackbody radiance at 10.6° C. Below 750 cm^{-1}, the suppression efficiency is degraded due to the dissymmetry in the absorption of the two ZnSe

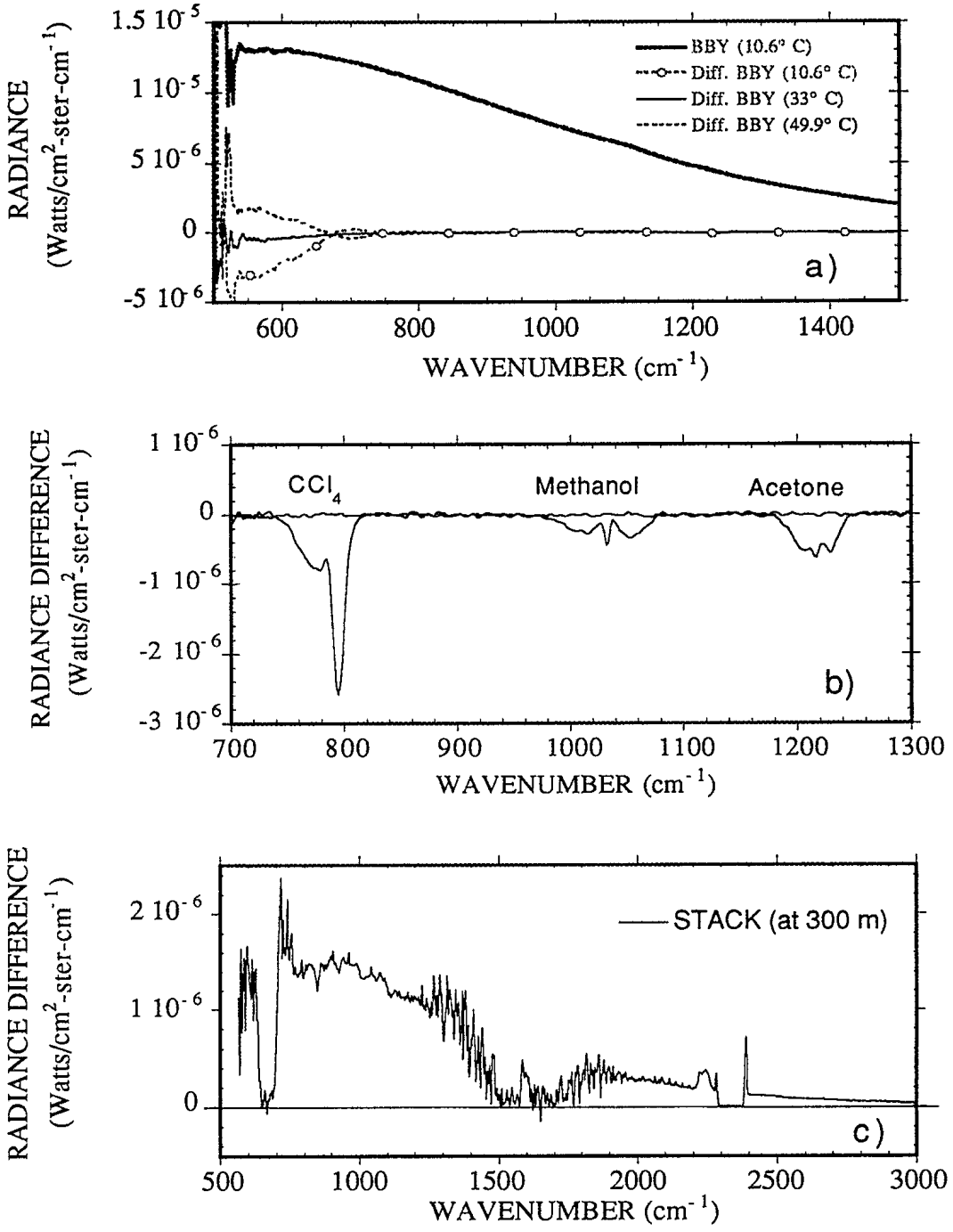

FIGURE 20 - Three examples of differential measurements with CATSI: for three different blackbody source temperatures (a), for three different chemical vapors (b) and for a smoke stack at 300 m (c)

substrate (and AR coatings) composing the beamsplitter. As seen in Section 5.3, this strong instrument residual can be properly predicted by eq. 120 (or 108).

The second series of laboratory measurements has been performed to study the evaporation characteristics of several chemical simulants (readily available) having IR absorption bands similar to some of the potential chemical threats. For that, a small-size vapor generator has been built to test experimentally the overall detection methodology. The actual vapor generator assembly is made of a 0.5-m long, 7.5 cm diameter pipe covering entirely a 100 ml becher containing the desired chemical in liquid form. The evaporation is efficiently realized by ventilation (no heating) using a small fan embedded in the middle of the pipe. This assembly produces a steady flow of chemical vapor at a concentration determined by the speed of the fan. Figure 20b shows superposed on the same graph the results of three distinct measurements performed on CCl_4, methanol and acetone vapors using the dual-beam interferometer operated in differential detection mode. For that, the two telescopes were aiming at different parts of the same flat plate blackbody (12"x12") which acts as a uniform background at a selected temperature of 44° C. The experimental set up was such that the generated vapor was probed by only one telescope and was covered entirely the FOV of the instrument. The vapor temperature was equal to the ambient temperature (approximately 24° C) providing a negative temperature contrast of 20° between the target vapor and the background. Figure 20b shows that in these conditions the three spectral signatures are easily and clearly identified. Note that for these results the small instrument residual (re_2) was removed for the sake of clarity. The spectra were recorded at a resolution of 4 cm^{-1} with a recording integration time of 4 seconds (30 scans).

The last measured example (4 cm^{-1} resolution) presented in Fig. 20c represents the radiance differential from the smoke stack of the DREV heating plant located approximately 300 meters from the receiver site. The observation is made at an elevation angle of ~1 degree having a cold clear sky as the background and an ambient temperature of -15° C. In Fig. 20b, the small instrument residual (re_2) was first measured independently and then subtracted from the measured signature. In this case, the radiance differential exhibits a rather conventional smoke stack signature with a strong blackbody emission coming from the hot parts of the stack. In addition, the so-called red and blue spikes associated with hot CO_2 emissions (edges of the 2350 and 650 cm^{-1} bands) are clearly observed together with the strong emission lines of hot water vapor in the 1200 to 1900 cm^{-1} region. Others spectral features in the 800-1200 cm^{-1} would require a deeper analysis to be associated with real

species or to a spectral background mismatch between the two adjacent scenes used for the differential detection.

7.0 SUMMARY AND CONCLUSIONS

An improved configuration of FTIR spectrometer for the remote detection of vapor IR emissions has been proposed. The originality of the approach lies in the use of a double-beam interferometer optimized for optical subtraction. This double-beam configuration is particularly suited for target differential detection where the simultaneous suppression of background and self-instrument contributions is done optically and in real time. Another advantage is that the proposed FTIR spectrometer requires only the monitoring of instrument temperatures to generate a radiometrically calibrated spectrum in real time, which represents a definite advantage over usual FTIR instruments .

The optimum FTIR spectrometer configuration has been quantitatively defined to fulfill three design conditions, i.e. balanced responsivities (input-1 vs input-2), balanced emissions (input-1 vs input-2), and beamsplitter transparency. To achieve these requirements we have proposed a fully symmetrical double-beam interferometer with a special beamsplitter assembly. The beamsplitter is made of an optically thin layer of air squeezed between two thick ZnSe substrates properly covered with antireflection coatings on their external faces.

To verify the proposed configuration, a prototype referred to as the Compact Atmospheric Interferometer Sounder (CATSI) has been developed according to the above specifications,. Results obtained with CATSI have shown that the instrument residual is not exactly zero but usually smaller than 2 % in the region from 700 to 3000 cm^{-1} (3.5-15 μm). However, an unexpected strong residual has been found in the region from 500 to 700 cm^{-1} (15-20 μm). After analysis it appears that these imperfections comes from the limited performance of the manufactured beamsplitter. In the strong-residual region (15- 20 μm), these imperfections are partly due to non-identical antireflection coatings present on the external face of each substrate and partly due to a difference between the transmission associated with each substrate. Both effects introduce a dissymmetry in the self-emission and the attenuation associated with each inputs. A simple model which predicts the instrument residual in terms of the substrate characteristics has been utilized to explain the observed residual. In the 2%-residual region (3.5-15 μm) it has been shown, based on a simple model,

that the observed channel spectra can be explained by a thickness mismatch of the order of 20 μm between the two ZnSe substrates forming the beamsplitter.

The experimental results obtained with the CATSI prototype have shown a background suppression factor of approximately 98% in the spectral region from 3.5 to 13 μm. The differential detection capabilities of CATSI have been illustrated in two ways. First to evaluate a smoke stack (heating plan) located at approximately 300 meters from the reception site, and second to evaluate the evaporation characteristics of three different chemicals: CCl_4, methanol and acetone vapors. Based on these measurements, the sensitivity of CATSI to acetone concentrations has been estimated. Future work will be oriented to the development of the differential detection method for the remote monitoring of target vapors and to field validations with the CATSI prototype.

8.0 ACKNOWLEDGMENTS

The author would like to thank Dr. Luc Bissonnette for many helpful suggestions related to this work. The expert technical assistance of Claude Bradette throughout this work is gratefully acknowledged.

9.0 REFERENCES

1. Kroutil, R. T., Combs, R. J., Knapp, R. B. and Godfrey, J. P., " Infrared Interferogram Analysis for Ammonia Detection with Passive FT-IR spectrometry ", Proceedings of the SPIE Conference on Electro-optical Technology for Remote Chemical Detection and Identification, Orlando 1996, SPIE Vol. 2763, 86, 1996.

2. Flanigan, D. S., " Prediction of the Limits of Detection of Hazardous vapors by Passive Infrared with the use of MODTRAN", Appl. Opt., vol. 35, 6090, 1996.

3. Althouse, M. L. G., Gross, R. L., Ditillo, J. T., Lagna, W. M., Koledzey, S. J., Keiser, C. C., and Nasers, G. D., " Applications and testing of the LSCAD system ", Proceedings of the SPIE Conference on Electro-optical Technology for Remote Chemical Detection and Identification, Orlando 1996, SPIE Vol. 2763, 33 1996.

4 Thériault, J.-M., " Fourier-transform Spectrometer Configuration Optimized for Self-emission Suppression and Simplified Radiometric Calibration", Submitted for Patent Application, September 15, 1997

5. Thériault, J.-M., Bradette, C., Villemaire, A., Chamberland, M. and Giroux, J., " Differential Detection with a Double-beam Interferometer ", Proceedings of the SPIE Conference on Electro-optical Technology for Remote Chemical Detection and Identification, Orlando 1997, SPIE Vol. 3082, 65, 1997.

6. Vanasse, G. A., " Spectrometric techniques ", Volume III, Academic Press, New York, 1983.

7. Revercomb, H. E., Buijs, H., Howell, H. B., Laporte, D. D., Smith, W. L. and Sromovsky, L. A., " Calibration of IR Fourier Transform Spectrometers: Solution to a Problem with the High-Resolution Interferometer Sounder " Appl. Opt., Vol. 27, 3210, 1988.

8. Heavens, O. S., " Optical Properties of thin Solid Films ", Dover Publications, Inc., New York, 1965.

INTERNAL DISTRIBUTION

DREV R-9804

1 - Deputy Director General
1 - Chief Scientist
6 - Document Library
1 - J.-M. Thériault (author)
1 - G. Otis
1 - J.-M Garneau
1 - C. Carrier
1 - L. Bissonnette
1 - D. Dion
1 - J. Cruickshank
1 - P. Chevrette
1 - T. Smithson
1 - G. Roy
1- D. St-Germain
1 - J.-P. Ardouin
1 - C. Bradette

EXTERNAL DISTRIBUTION

DREV R-9804

1 - DRDIM
1 - DRDIM (unbound copy)
1 - DRDB
1 - DSAA
1 - DGMetOc
1 - DSACCIS
1 - DSAM
1 - DSAL
1 - DSAA
1 - DMSS
1 - DSSPM
1 - DASPM
1 - DAEPM(C)

2 - Ms. G. P. Anderson & Dr. A. Ratkowski
Phillips Laboratory
Geophysics Directorate (PL / GPOA)
Hanscom AFB
MA 01731
U.S.A.

2 - Dr. R. Kroutil (SCBRD-RT) &
Mr. R. J. Combs (SCBRD-RT E5951)
US Army ERDEC
5232 Fleming Road
Aberdeen Proving Ground, MD 21010-5423
U.S.A.

1- Dr. B.D. Billard
Naval Surface Warfare Center
White Oak Laboratory
Code R42
Silver Spring, MD 20903-5000
U.S.A.

1 - Dr. T. Jones
U.S. Army Night Vision & Electro-optics
Laboratory
DELNV-VI
Fort Belvoir, VA 22060
U.S.A.

1 - Mr. R.K. Redfield
Department of the Army
Cold Regions Research & Engineering
Laboratory
Corps of Engineers
Hanover, NH 03755
U.S.A.

1 - M. A.P. Junchat
CELAR-Centre d'électronique d'armement
Division ASRE
35170 Bruz
France

1 - Dr. A. Kohnle
Forschungsinstitut für Optik (FfO)
Schloss Kressbach
74 Tübingen
Federal Republic of Germany

1- Dr. G. de Leeuw
Physics Laboratory FEL-TNO
Oude Wallsdorperweg 63
2597 AK, The Hague
Netherlands

DOCUMENT CONTROL DATA

1. ORIGINATOR (name and address) Defence Research Establishment Valcartier 2459 Pie XI Blvd, North Val-Bélair, Québec G3J 1X5	2. SECURITY CLASSIFICATION (Including special warning terms if applicable) UNCLASSIFIED

3. TITLE (Its classification should be indicated by the appropriate abbreviation (S,C,R or U)
IR Fourier Spectrometer for Differential Detection: Design, Prototype and Results (U)

4. AUTHORS (Last name, first name, middle initial. If military, show rank, e.g. Doe, Maj. John E.)

Thériault, Jean-Marc

5. DATE OF PUBLICATION (month and year)	6a. NO. OF PAGES	6b. NO. OF REFERENCES

7. DESCRIPTIVE NOTES (the category of the document, e.g. technical report, technical note or memorandum. Give the inclusive dates when a specific reporting period is covered.)

Technical Report

8. SPONSORING ACTIVITY (name and address)

9a. PROJECT OR GRANT NO. (Please specify whether project or grant)	9b. CONTRACT NO.

10a.ORIGINATOR'S DOCUMENT NUMBER	10b. OTHER DOCUMENT NOS.
	N/A

11. DOCUMENT AVAILABILITY (any limitations on further dissemination of the document, other than those imposed by security classification)

- [X] Unlimited distribution
- [ ] Contractors in appoved countries (specify)
- [ ] Canadian contractors (with need-to-know)
- [ ] Government (with need-to-know)
- [ ] Defence departments
- [ ] Other (please specify) :

12. DOCUMENT ANNOUNCEMENT (any limitation to the bibliographic announcement of this document. This will normally correspond to the Document Availability (11). However, where further distribution (beyond the audience specified in 11) is possible, a wider announcement audience may be selected.)

Unlimited

13. ABSTRACT (a brief and factual summary of the document. It may also appear elsewhere in the body of the document itself. It is highly desirable that the abstract of classified documents be unclassified. Each paragraph of the abstract shall begin with an indication of the security classification of the information in the paragraph (unless the document itself is unclassified) represented as (S), (C), (R), or (U). It is not necessary to include here abstracts in both official languages unless the text is bilingual).

This report presents the theoretical basis and validation measurements supporting a new configuration of Fourier-transform IR spectrometer optimized for differential detection. The optimized configuration exploits the optical subtraction capabilities of a double beam Michelson interferometer to achieve the suppression of the spectral background. The resulting configuration is a fully symmetrical FTIR double beam interferometer with a peculiar beamsplitter assembly. Results obtained with a prototype indicate a high level of suppression with a residual usually smaller than 2% in the spectral range from 3.5 to 15 μm. Finally, it is shown that such a spectrometer configuration allows a permanent radiometric calibration which represents a definitive advantage over conventional FTIR instruments.

14. KEYWORDS, DESCRIPTORS or IDENTIFIERS (technically meaningful terms or short phrases that characterize a document and could be helpful in cataloguing the document. They should be selected so that no security classification is required. Identifiers, such as equipment model designation, trade name, military project code name, geographic location may also be included. If possible keywords should be selected from a published thesaurus. e.g. Thesaurus of Engineering and Scientific Terms (TEST) and that thesaurus-identified. If it is not possible to select indexing terms which are Unclassified, the classification of each sould be indicated as with the title.)

Passive Remote Sensing

Infrared Spectra

FTIR Spectrometer

Differential Detection

Double Beam Interferometer

UNCLASSIFIED

Requests for documents
should be sent to:

DIRECTORATE RESEARCH AND DEVELOPMENT
INFORMATION MANAGEMENT
Dept. of National Defence
Ottawa, Ontario
K1A 0K2

Tel.: (613) 995-2971
Fax: (613) 996-0392

#308328

Toute demande de document
doit être adressée à:

DIRECTEUR-GESTION DE L'INFORMATION DE RECHERCHE
ET DE DÉVELOPPEMENT
Ministère de la Défense nationale
Ottawa, Ontario
K1A 0K2

Téléphone: (613) 995-2971
Télécopieur: (613) 996-0392

SANS CLASSIFICATION